



A nonlinear inversion method for predicting the in-situ stress field in deep coal seam based on improved long short-term memory neural network

Jiaxing Zhou^{a,b,c}, Bisheng Wu^{a,b,c,*}, Yuanxun Nie^{a,b,c}, Haitao Zhang^{a,b,c}

^a State Key Laboratory of Hydroscience and Engineering, Tsinghua University, Beijing, 100084, China

^b Department of Hydraulic Engineering, Tsinghua University, Beijing, 100084, China

^c Key Laboratory of Hydrosphere Sciences of the Ministry of Water Resources, Tsinghua University, Beijing, 100084, China



ARTICLE INFO

Keywords:

In-situ stress field
Discontinuous
Nonlinearity
Improved LSTM algorithm

ABSTRACT

Existence of discontinuous geological structures, such as folds and fault, poses a great challenge in predicting the in-situ stress fields (ISSF). This paper proposes a discontinuous intelligent inversion method to predict the ISSFs in the deep coal seam area (DCSA) of the Shanghai Temple, which exhibits distinct discontinuous geological features. The proposed method consists of three key components. First, a discontinuous loading model was developed to address the problem of accuracy in the numerical simulation of discontinuous tectonic regions such as folds and faults. The simulation data generated is used as a sample dataset for the training of the inversion algorithm and their completeness is fully guaranteed. Second, the statistical distribution patterns of horizontal, maximum and minimum lateral pressure coefficients (LPCs) of the ISSF in the typical DCSAs of China is statistically calculated. By applying Gaussian- and Cauchy-type fuzzy membership functions, the degree of influence of faults and folds on the local ISSF is quantified and the geological structure influence model is constructed. The influence value enriches the input data dimension of the algorithm and lays a more detailed data foundation for the stress inversion. Third, the improved Long Short-Term Memory (LSTM) network algorithm was constructed by optimizing the network hierarchy and multi-parameter cyclic learning. An inversion analysis is carried out using the ISSF around the borehole as an example, and the relative error strictly controlled within 1 %. The improved LSTM algorithm achieves an accuracy of 88.58 % at each measurement point in the Shanghai Temple deep coal seam project, which is significantly higher than that of the back propagation neural network (BPNN). The discontinuous intelligent inversion method proposed in this study can provide an effective tool for predicting the ISSF in DCSA.

1. Introduction

The shallow coal resources are becoming increasingly depleted, prompting a shift towards deep coal resources within a depth range of 500~1500 m, which has emerged as a focal development direction in the energy field.¹⁻³ The geological body within this burial depth range primarily originated in the Palaeozoic era, including the Silurian, Ordovician, and Mesozoic periods. These formations have undergone intense tectonic movements, including the Caledonian, Hercynian, Indosinian, and Yanshan movements, forming extensive and intricate geological structures such as folds and faults and enhancing the discontinuity between sedimentary layers.^{4,5} When the mining depth of discontinuous structural coal seam exceeds 500 m, the working face area disasters are frequent, such as the large scale disintegration of rock

masses,^{6,7} the failure mode of rock from brittleness to ductility, the exponential increment of rock burst and mining-induced seismicity,^{8,9} seriously affecting mining efficiency and quality.¹⁰ The complex distribution of ISSF is the primary factor causing disasters. A good understanding of the ISSF in mining areas provides a foundation for addressing these problems and ensuring safe and efficient mining.¹¹⁻¹³ As it is very difficult to accurately obtain the distribution of the ISSFs in the DCSA due to complex geological settings using conventional approaches, developing an intelligent algorithm that can make a reasonable prediction of the ISSFs in the DCSA with limited field data is of great significance for assessing the stability of coal seams and ensuring the safe production of mines.

The methods for obtaining the ISSFs are mainly divided into three types, i.e. field measurement method, lateral pressure coefficient

* Corresponding author. Department of Hydraulic Engineering, Tsinghua University, Beijing 100084, China.

E-mail address: wu046@mail.tsinghua.edu.cn (B. Wu).

method and inversion calculation method. Field measurement is one of the most direct ways to obtain the ISSF, such as hydraulic fracturing tests, strain relief methods, acoustic emission technology, but it is often a difficult, expensive and frustrating task, and not suitable to be used on a large scale in engineering.^{14,15} The lateral pressure coefficient method is a direct calculation method for determining in-situ stress. It calculates the vertical stress at a point by determining the weight of the overburden and estimates the horizontal stress based on the Poisson's ratio of the rock.¹⁶ This method is simple and easy to perform suitable preliminary estimation of the ISSF. Inversion calculation is a commonly used method for inferring the ISSF, and it can achieve high accuracy for shallow geological layers. However, when it comes to the discontinuous areas in deep coal seams, this method faces multiple challenges. First, during the process of rock formation, the widespread discontinuous geological structures, such as faults and folds caused by multiphase, nonlinear and discontinuous tectonic movements, lead to abrupt changes and anomalies in the regional ISSF. Second, deep rock masses are significantly affected by the coupling of temperature and seepage, exhibiting pronounced nonlinear mechanical behavior, which diminishes the regularity of the ISSF in different regions.^{17,18} Third, the influence of deep geological conditions on field measurement equipment poses challenges in data collection, leading to a higher degree of measurement uncertainty. Last, when faced with scarce and discrete measured sample data, there are challenges in the adaptability of inversion models and algorithms, making effective learning difficult. In view of the complexity of the ISSF in deep coal seam areas (DCSA), developing an intelligent inversion method that integrates geomathematical analysis and deep learning algorithms is particularly critical.

In the field of intelligent inversion research, scholars have made significant breakthroughs in inferring the ISSF by applying machine learning algorithms. They have integrated a variety of models including neural networks, surrogate models, ensemble learning, and full leveraging the unique advantages and characteristics of each models.^{19,20} QIAN et al. used the generative adversarial network (GAN) algorithm, inputting the depth, position, and lateral pressure coefficient of measurement points, to output the load coefficient of the geological model, significantly improving the accuracy of ISSF inversion.²¹ Song et al. predicted the ISSF distribution in the thick coal seam in the Licun by using a BPNN model.²² The result confirms the effectiveness and accuracy of the BPNN for stress inversion under complex geological conditions. This demonstrates the great potential of neural network models in enhancing the inversion accuracy in geological data processing. Li et al. proposed an intelligent inversion method based on surrogate model-accelerated random search, effectively combining random search with surrogate models to expedite the convergence of global optimization problems, providing precise results for the stress distribution in underground mines in Pennsylvania.²³ PEI et al. integrated the finite difference method (FDM) and the discrete element method (DEM) to develop a two-stage intelligent inversion method, which provided an in-depth analysis of the ISSF in deep discontinuous structural areas.²⁴ Furthermore, ZHANG et al. developed an integrated learning inversion method by combining stepwise regression (SR), differential evolution (DE), support vector machine (SVM), and numerical analysis techniques, demonstrating higher accuracy in predicting the ISSF.²⁵ In the field of regression analysis models, YU et al. used the partial least squares regression to fit the ISSF, improving the fitting accuracy for the areas with local stress anomaly by regressing each stress component separately.²⁶ MENG et al. proposed a ridge regression method for inverting the ISSF, analyzing the inversion examples of the ISSF in the Banzhulin tunnel rock mass, deeply explored the impact of multicollinearity on the regression coefficients, and optimized the inversion process to enhance the accuracy of the results.²⁷ Looking further at the ISSF inversion results in the aforementioned examples, there exist two areas with relatively low ISSF inversion accuracy. First, the pattern of mutation distribution of the ISSF at the interface of the fault fracture zone and its surrounding rocks is not obvious.^{28,29} Second,

the ISSF in the formations with fold structure lacks clear bounding zones for stress enhancement or attenuation.³⁰ These error features show the complexity of the ISSF in DCSA, and directly reflect the accuracy bottleneck faced by the most algorithms in inferring the deep ISSF.

To fully exploit the geological information in the measurement area and improve the inversion accuracy of the ISSF, this study integrates geological analysis, numerical modelling, and improved LSTM algorithm model to establish an intelligent inversion method for inferring the ISSF in discontinuous DCSA regions (hereafter referred to as the “discontinuous intelligent inversion method”). Through the validation of the ISSF of rock mass around a deep borehole as an example, the developed algorithmic model exhibits a high prediction accuracy with an error rate of less than 1 %. Meanwhile, with regard to the distribution characteristics of the ISSF in the DCSA of Shanghai Temple, the discontinuous intelligent inversion method proposed by this study realizes the significant improvement of the overall inversion accuracy of the ISSF, which fully verifies its effectiveness and reliability in the analysis of the ISSF in DCSA.

2. Statistical analysis and numerical model construction of ISSF in deep coal mines in China

2.1. Basic framework of discontinuous intelligent inversion methods

The discontinuous intelligent inversion method consists of three key components, i.e. application of discontinuous loading condition on the geological model (hereinafter referred to as “discontinuous loading model”), use of a fuzzy membership function to quantify the influence of geological tectonic on the ISSF (hereinafter referred to as “geological structure influence model”), and improvement of long short-term memory network (referred to as “improved LSTM algorithm”).

First, to address the generalization limitations of geological models due to scale differences and the impact of the complexity of multi-phase tectonic movements in geological history on the accuracy of numerical simulation of the ISSF, the discontinuous loading model is developed by focusing on discontinuous geological tectonic regions such as folds and faults. The model imposes three types of discontinuous loading conditions, namely compression, shear and self-gravity, which accurately simulate the characteristics of local variations of the ISSF in the tectonic region. The generated simulation data are used as a sample dataset for the training of the inversion algorithm and their completeness is fully guaranteed.

Second, to investigate the influence of folds and faults on the local ISSF and the difficulty of comprehensively capturing the geological characteristics of the whole region with limited measurement data, the statistical distribution patterns of the horizontal, maximum and minimum LPCs of the regional ISSF in the DCSA of China were statistically calculated. By applying the Gaussian and Cauchy-type fuzzy membership functions, the degree of influence of faults and folds on the local ISSF is quantified and the geological tectonic influence degree function is constructed. The geological tectonic influence value not only enriches the input data dimension of the inversion algorithm, but also lays a more detailed data foundation for the inversion calculation process.

Third, considering the sample dataset such as the location of measuring points, ISSF data, and the influence of geological structure on the ISSF, the improved Long Short-Term Memory (LSTM) network algorithm was constructed to improve the algorithm's ability to handle large-scale and high-complexity regional geological data of the DCSA by optimizing the network hierarchy and multi-parameter cyclic learning.

2.2. Statistical analysis of the ISSF in the DCSA of China

The mathematical analysis of the ISSF in the DCSA consists of two aspects. First, 230 sets of representative ISSF data from measuring points of deep coal mines in China were collected, and the Hoek-Brown statistical method was applied to determine the quantitative equations for

the change pattern and distribution range of ISSF with depth. These equations are crucial for the preprocessing the sample dataset and the construction of the input metrics in the inversion algorithm, which can guarantee the accuracy and stability of the algorithm. Second, in the numerical calculations, three types of discontinuous loading conditions were used, i.e. compressive loading, shear loading and self-weight loading. By imposing these loading conditions on the geological model, the resulting discontinuous loading model is able to characterize the locally complex nonlinear and discontinuous properties in the ISSF. The numerical results of the discontinuous loading model ensure the reliability and integrity of the sample dataset.

In the paper, a total of 230 sets of ISSF data measured from several coal mining regions in China are collected, as listed in Table 1. The distribution of the ISSF data basically covers the main coal mining areas in mainland China.

With reference to the Hoek-Brown in-situ stress analysis,^{31,32} three types of LPCs are considered in this study. The maximum, minimum and average horizontal LPCs, i.e. K_H , K_h , K_{av} , are defined as the maximum, minimum and average horizontal principal stresses divided by the vertical stress. Taking the average horizontal LPC as an example, the scattered plots of the inner and outer fitting and all measurement point data are shown in Fig. 1, where $K_{av, Ho}$ and $K_{av, o}$ are the outer fitting functions for the Hoek-Brown and the DCSA statistics, and $K_{av, Hi}$ and $K_{av, i}$ are the inter fitting functions for the Hoek-Brown and DCSA statistics (see Fig. 1).

Based on the extensive statistical data of the measured ISSF, the average LPC in the DCSA of China shows a greater variability than the Hoek-Brown statistical data. This is mainly due to the influence of multi-stage geological movements, intermittent stratigraphic deposits, and widely distributed geological formations during the tectonic history.^{27,33} There is a certain degree of competition relationship between the horizontal and vertical ISSF, and there are three types of ISSF distribution in the localized geologic body, i.e. strike-slip fault type ($\sigma_H > \sigma_h > \sigma_v$), reverse fault type ($\sigma_H > \sigma_v > \sigma_h$), and positive fault type ($\sigma_v > \sigma_H > \sigma_h$).³⁴ Where σ_H and σ_h are the maximum and minimum horizontal principal stresses, and σ_v is the vertical principal stress.

By using a regression analysis, the variation of the ISSF with burial

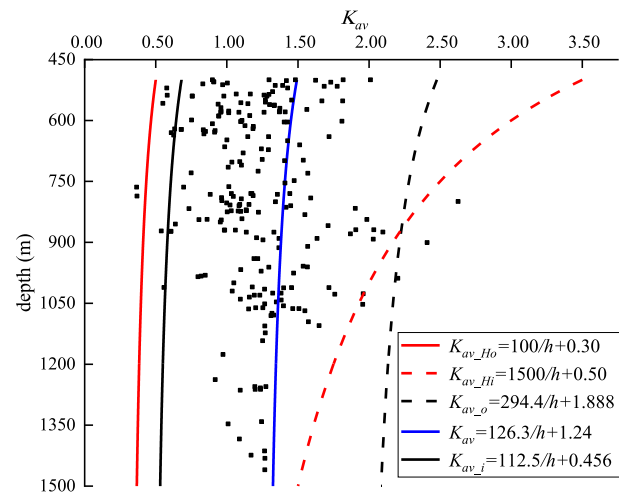


Fig. 1. Variation of the average LPC with depth in DCSA.

depth in the DCSA of China is determined, and the regression equations describing the average, maximum, and minimum horizontal LPCs were shown as follows

$$K_{av} = \frac{126.3}{z} + 1.24 \quad (1)$$

$$K_H = \frac{164.8}{z} + 1.525 \quad (2)$$

$$K_h = \frac{-187.5}{z} + 1.186 \quad (3)$$

Here z denotes the burial depth in m.

In order to quantify the ISSF distribution in the DCSA of China, the equations for the inner and outer fitting of the average, maximum, and minimum horizontal LPCs are shown as follows by ensuring that at least 95 % of the measured data points fit closely within the ranges defined by these fitting

$$\frac{112.5}{z} + 1.240 \leq K_{av} \leq \frac{294.4}{z} + 1.888 \quad (4)$$

$$\frac{233}{z} + 0.447 \leq K_H \leq \frac{261.3}{z} + 2.61 \quad (5)$$

$$\frac{57.66}{z} + 0.347 \leq K_h \leq \frac{390.9}{z} + 1.099 \quad (6)$$

where the equations on the left side denote the inner fitting equations, while those on the right side denote the outer fitting equations.

2.3. Discontinuous loading model for the ISSF in the DCSA

The intelligent inversion of the ISSF consists of three steps. First, a geological model that closely matches the actual conditions is developed. Second, numerical calculations are performed by applying different loading conditions in the geological model to construct a complete sample data set; Third, an efficient inversion algorithm is used to invert the loading conditions that are most consistent with the actual geological tectonic movement. The accuracy of the ISSF inversion is highly dependent on a key step in the numerical simulation: ensuring that the loading conditions imposed on the geologic model accurately simulate the complexity of the actual geotectonic movements.³⁵ When the previous ISSF inversion practices were performed, it was clearly seen that the ISSF inversion results for shallow, continuous strata exhibited a high accuracy when using continuous loading conditions on geologic

Table 1
Sources and basics of statistical ISSF.

| Mining area | Number of points | Minimum depth/m | Maximum depth/m | Measurement Methods |
|--------------------|------------------|-----------------|-----------------|----------------------|
| Huainan Mine | 42 | 505 | 1450 | Hydraulic fracturing |
| Juye Mine | 37 | 791 | 1105 | Hydraulic fracturing |
| Duerping Mine | 3 | 463 | 630 | Hydraulic fracturing |
| Xishan Mine | 2 | 622 | 636 | Hydraulic fracturing |
| Binchang Mine | 57 | 536 | 954 | Stress relief method |
| Shuangyashan Mine | 14 | 501 | 699 | Stress relief method |
| Shanghaimiaoz Mine | 12 | 501 | 703 | Hydraulic fracturing |
| Xieqiao Mine | 7 | 920 | 920 | Stress relief method |
| Xinli Mine | 3 | 750 | 800 | Stress relief method |
| Luling Mine | 3 | 615 | 975 | Stress relief method |
| Guotun Mine | 4 | 806 | 855 | Stress relief method |
| Songshan Mine | 3 | 598 | 611 | Stress relief method |
| Haishiwan Mine | 4 | 750 | 950 | Stress relief method |
| Hongqingliang Mine | 3 | 488 | 500 | Stress relief method |

model (hereinafter referred to as the ‘continuous loading model’). However, continuous loading models shows a significant decrease in the inversion accuracy of the ISSF when dealing with regions with discontinuous geological structures such as faults and folds.²¹

The main problem lies in the limitations of the local generalisation zones of geological model and effect of the variability of the multi-phase geotectonic movements. First, the simulation results of the continuous loading model can characterize the uniform variation of ISSF on a large scale, but it is difficult to characterize the nonlinear and locally discrete properties of ISSF in complex geological formations with faults and folds. In particular, due to scale limitations, the accuracy of ISSF calculations for continuum loading model is significantly reduced in areas of geological formations that have to be generalized in the geological model. Second, the type and intensity of tectonic movements varied during different gyrations in the course of geological history, and it was difficult for the continuity loading model to capture the sudden changes and phases of tectonic movements. Continuum loading model cannot guarantee the accuracy and reliability of full-domain simulation results due to their intrinsic limitations. This deficiency directly affects the ability to generate complete and accurate sample datasets that are essential for the effective operation and accurate resolution of inversion algorithms.

In order to accurately simulate the complexity of the actual geological tectonic movement, the compression, shear and self-weight loading conditions as shown in Fig. 2 are imposed on the geological model, and the discontinuous loading model is thus constructed. By using the Taylor's formula, only the first three terms are used as approximation for the loading equations, which efficiently ensures the computational accuracy of the discontinuous loading model and maintains the simplicity of the calculation. The specific mathematical expressions are shown in Eqs. (7)–(9). Particularly important is that the three types of loading equations employ a multiband function form, which enables the loading conditions to characterize the local variations in the ISSF within geological structural regions.

Using the burial depth as the independent variable, the compressive loading equation takes a segmented quadratic form as follows

$$P_x(z) = p_{0,i} + p_{1,i}z + p_{2,i}z^2 \quad z \in [z_i^{(x)}, z_{i+1}^{(x)}] \quad (7)$$

where P_x is the compressive loading function along the X -axis in the geologic model in Pa ; $z_i^{(x)}$ and $z_{i+1}^{(x)}$ denote the minimum and maximum coordinates in vertical direction (Z -axis direction) of the i -th compression loading partition in m, respectively; $p_{0,i}$, $p_{1,i}$ and $p_{2,i}$ are fitting coefficients for function in the i -th load partition. It can be seen that by independently parameterizing the quadratic function in different partition, the loading condition is able to accurately characterize the complex variations in tectonic movements at different depths.

In addition, the compressive loading equation can be further segmented according to the horizontal coordinates. This allows the loading condition to account for differences in compressive tectonic motion in the horizontal direction between different geotectonic regions, thus enabling more refined and region-specific load distribution simulations.

Similarly, with the burial depth as the independent variable, the shear loading equation takes a segmented quadratic form as follows

$$T_{xy}(y, z) = t_{0,i} + t_{1,i}z + t_{2,i}z^2 \quad z \in [z_i^{(xy)}, z_{i+j}^{(xy)}], y \in [y_i^{(xy)}, y_{i+1}^{(xy)}] \quad (8)$$

where T_{xy} is the shear loading function, which specifies the shear loading action along the Y -axis at an interface perpendicular to the X -axis. $z_i^{(xy)}$ and $z_{i+j}^{(xy)}$ denote the minimum and maximum coordinates, respectively, of the i -th shear loading partition in the vertical direction (Z -axis direction); $y_i^{(xy)}$ and $y_{i+1}^{(xy)}$ denote the start and end coordinates of the i -th shear loading partition in the Y -axis direction, respectively. $t_{0,i}$, $t_{1,i}$ and $t_{2,i}$ are fitting coefficients for function in the i -th load partition.

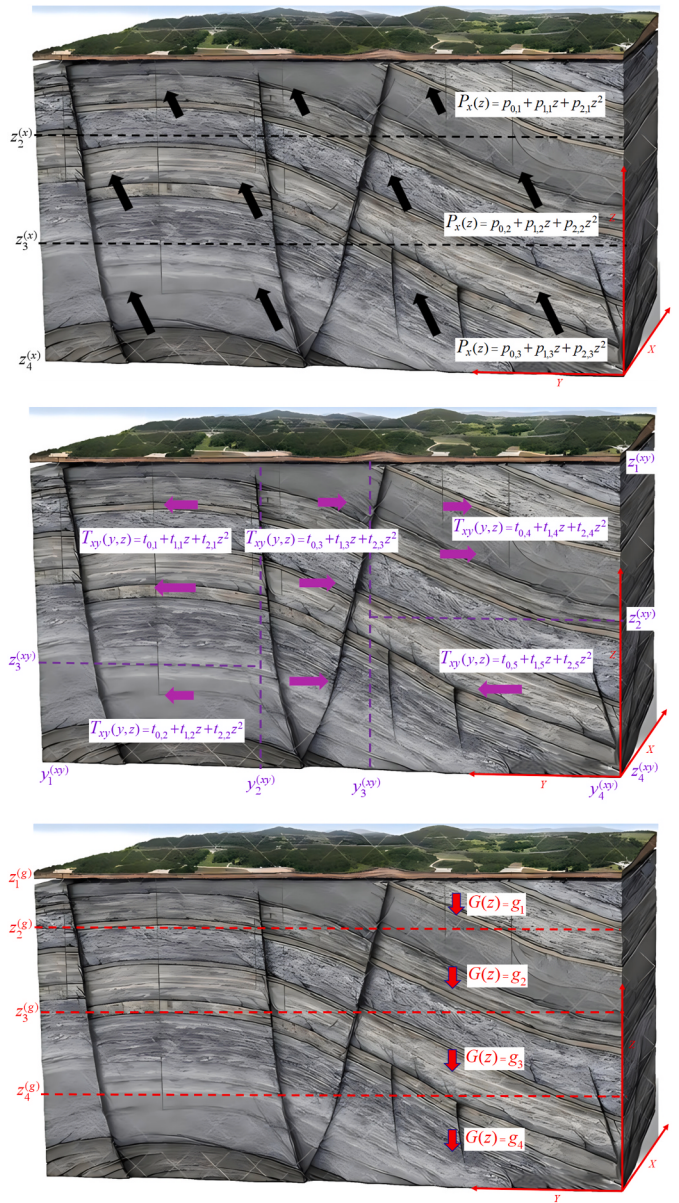


Fig. 2. Schematic diagram of nonlinear and discontinuous boundary loads.

By adjusting the parameters of the quadratic function to adapt to the tectonic characteristics of different regions, the loading condition significantly improves its ability to simulate the differences in complex tectonic movements in the horizontal direction for different geologic regions.

The self-weight loading equation takes the form of a segmented function along the depth of burial, i.e.

$$G(z) = \begin{cases} g_1 & z \in [z_1^{(g)}, z_2^{(g)}] \\ g_2 & z \in [z_3^{(g)}, z_4^{(g)}] \\ \vdots & \\ g_n & z \in [z_{2n-1}^{(g)}, z_{2n}^{(g)}] \end{cases} \quad (9)$$

where g_1 , g_2 , and g_n are the equivalent gravitational accelerations of each generalized rock layer, respectively. $z_{2n-1}^{(g)}$, and $z_{2n}^{(g)}$ denote the minimum and maximum vertical coordinate values of the n -th gravity equivalent layer. The self-weight loading condition is characterized by constant loads within each segment and varying loads across different

segments.

3. Improved LSTM algorithm

When exploring the improved LSTM algorithm, the focus is put on the optimization of two core areas. First, regarding the statistical laws of the three types of LPCs in Section 2.2, by introducing the fuzzy membership function to quantify the degree of influence of folds and faults on the ISSF of the measurement point. In view of this, the geological structure influence model has been developed, which calculates the degree of influence of geological structures on the ISSF in a specific measurement point area, using the three LPCs as independent variables. This type of influence degree values not only enriches the input data dimensions of the algorithmic model, but also lays a more detailed data foundation for the inverse calculation process. Second, for the improvement of the algorithm topology, it is committed to enhancing the intrinsic performance and adaptive ability of the algorithm model. By means of optimizing the network hierarchy and multi-parameter cyclic learning, the algorithm enhances its ability to handle large-scale and high-complexity data.

3.1. Construction of geotectonic influence degree input values based on fuzzy membership function

According to the statistical results of ISSF data in the literature,^{35–37} the in situ stress at the end of faults is significantly larger than that in adjacent areas, while the in situ stress within fault zones is smaller than that in nearby regions. When a fault stabilizes, the maximum horizontal principal stress usually aligns with the fault strike, while the minimum horizontal principal stress is perpendicular to the fault strike. Faults exert an influence on the ISSF through various mechanisms, including stress concentration, stress release and displacement changes. Fracture structures, such as weak zones in the Earth's crust, are prone to stress concentration and release, resulting in intense stress gradients near the fault zones. However, the scale of this influence is relatively small, and it gradually diminishes as the distance from the fault zone increases. On the other hand, stress concentration in the folded structures is evident in the axial partition of the synclines, where the horizontal stresses are significantly larger than vertical stresses and also greater than the horizontal stresses in the limbs. The folds influence the ISSF by altering stress distributions, generating strain hardening, and introducing tectonic stresses, resulting in relatively minor changes in the ISSF but with a relatively large scale of influence.

In view of this, according to the method of defining membership functions in fuzzy theory,^{38,39} using the average, maximum, and minimum horizontal LPCs as independent variables, the Gaussian-type distribution function is selected to quantify the degree of influence of faults on the ISSF in the area of the measurement point, and the Cauchy-type distribution function is selected to quantify the degree of influence of folds on the ISSF in the area of the measurement point.

The Gaussian-type distribution function used to characterize the degree of influence of the fault structure on the ISSF in the area near the measurement point is written as follows^{38,39}

$$\mu_1(k) = \frac{1}{1 + \alpha|k - k_0|^{-\beta}} \quad (10)$$

where μ_1 denote the degree of the influence of the fault structures on the ISSF at the measurement point, and the value range from 0 to 1. The larger value of μ_1 , the greater degree of influence of the ISSF at measurement point by the fault structure. k represents the three types of LPCs at the measurement points to be studied, and its average, maximum and minimum horizontal LPCs can be determined directly from the measured ISSF data. k_0 denotes the average value of the three types of LPCs at the depth of the measurement point to be studied, and its value is determined by the regression equation derived from the

statistical results in Section 2.2, as shown Eqs (1)–(3). α and β are the fitting coefficients, which are different for each measurement point. The extremum values of the LPCs were extracted based on the inner and outer fittings determined in Eqns. (4)–(6), with the corresponding extreme value being set to be 1, from which the fit coefficients can be calculated for each measurement point.

The Cauchy-type distribution function used to characterize the degree of influence of fold structure on the ISSF in the area around the measurement point is written as follows^{39,40}

$$\mu_2(k) = 1 - e^{-\theta|k - k_0|} \quad (11)$$

where μ_2 is the influence degree of the fold structures on the ISSF at measurement point, and the value range from 0 to 1. θ is the fitting coefficients, calculated in the same way as for the fault configuration.

In order to assess the combined effects of fault and fold structures on the ISSF in the area of the measurement point, a method based on the linear superposition principle is used. This method constructs the geological structure influence model by directly adding the influence of faults (calculated according to Eqn. (10) and the influence of folds (calculated according to Eqn. (11)). This model is able to quantify the overall extent of the effect of geological structures on the ISSF in the region

$$\mu(a, b, k) = b + \frac{a}{1 + \alpha|k - k_0|^{-\beta}} - be^{-\theta|k - k_0|} \quad (12)$$

where μ denotes the value of the degree of influence of regional geological structures on the ISSF at the measuring point, which can be used as an input to the algorithmic model, extending the input data dimension of the algorithmic model. a and b are the influence weight of fault and fold structures, respectively, and can be determined according to the geological conditions. It should be noted that their sum is 1. If the measurement point is situated within a fractured fault zone, a is set to be 1, while if the measuring point is located at the core and limb of a fold, b is set to be 1.

3.2. Topology of the improved LSTM algorithm

The improved LSTM algorithm utilizes the optimal learning strategy and error back propagation updating technique^{41,42} to combine the ISSF data at all measurement points, spatial locations and the geological tectonic influence values, to jointly form an input data sequence. The output of the algorithm is a discontinuous and nonlinear loading condition, which captures accurately the subtle changes in the geological tectonic movements and the effects of these changes on the distribution of the ISSF, thus realizing the accurate prediction of the ISSF.

In the core part of the algorithm, three nonlinear activation functions were selected, which were applied to different neurons in the algorithmic model, as follows

$$\tanh(x) = \frac{4}{(e^x + e^{-x})^2} \quad (13)$$

$$\sigma(x) = \frac{1}{1 + e^{-x}} \quad (14)$$

$$\tan(x) = \frac{e^x - e^{-x}}{e^x + e^{-x}} \quad (15)$$

where x is the input of the algorithm.

The three types of activation functions enhance the nonlinear handling of the algorithm model and enable it to better adapt to the complexity and diversity of geologic data. Fig. 3 shows the image characteristics of the three kinds of activation functions, and the function curves not only reveal the nonlinear transformation and activation process of the activation function on the input data, but also intuitively present the mapping relationship between the input and output values.

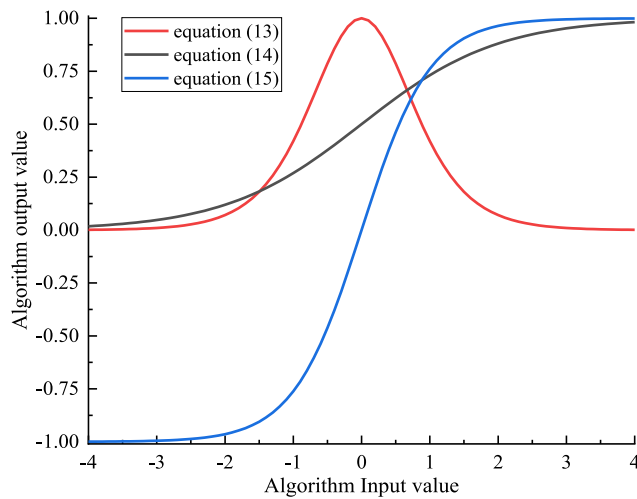


Fig. 3. Images of each activation function in the algorithm.

It is worth noting that the input and output values in Fig. 4 are set to be dimensionless numbers, and this design eliminates the limitation of data units, which makes the algorithm more flexible and versatile in dealing with geologic data of different magnitudes and from different sources.

The structure of the improved LSTM algorithm is shown in Fig. 4, where the algorithm model consists of one input layer, two hidden layers and one output layer. During data preprocessing, the sample data is normalized. For prediction datasets that fall outside the range of the training dataset, the entire dataset is re-normalized. The optimization of all parameters in the model relies on the error back propagation method, which ensures continuous optimization of model during training.⁴¹

In the first hidden layer, it is divided into five regions (① to ⑤), each of which contains 30 neurons for parallel processing and data feature diversification. The neurons in regions ① to ④ use the activation functions in the form of Leaky ReLU, which effectively mitigates the gradient vanishing problem by allowing small negative gradients to pass through, enhancing the nonlinear representation of the algorithm model. For the neurons in region ⑤, the HardTanh activation function was chosen, whose hard-limiting property introduces additional nonlinearities to the algorithm model, which helps in the information transfer of specific types of data.

On the basis of the first hidden layer, the second hidden layer and the output layer neurons mainly utilize nonlinear activation function, matrix operation and summation mechanism to deeply explore the intrinsic connection between the data features, and finally generate the output results with high prediction accuracy and practical value.

In the second hidden layer, it is divided into four regions (⑥ to ⑩), each of which also contains 30 neurons. The activation functions defined by Eqs. (13) and (14) are used in regions ⑥ to ⑨, respectively, which significantly enhance the algorithm model's ability to process complex geologic information data.⁴³ And the neurons in area ⑩ choose HardTanh activation function to realize the transmission of long-term memory information.

In the second hidden layer, the specific function form of the neuron in region ⑩ follows the following equation

$$f^{(n)} = \tanh\left(W_f^{(n)} \mu^{(n)} + U_f^{(n)} \Delta k^{(n)} + V_f^{(n)} \Delta h^{(n)} + b_f^{(n)}\right) \quad (16)$$

where $f^{(n)}$ is the output value of the measuring point n with respect to the neurons in region ⑩. $\Delta h^{(n)}$ is defined in three-dimensional space as a normalized measure of the change in position between a measurement point n and its previous measurement point. This data is derived by calculating the difference between the distances of two measurement

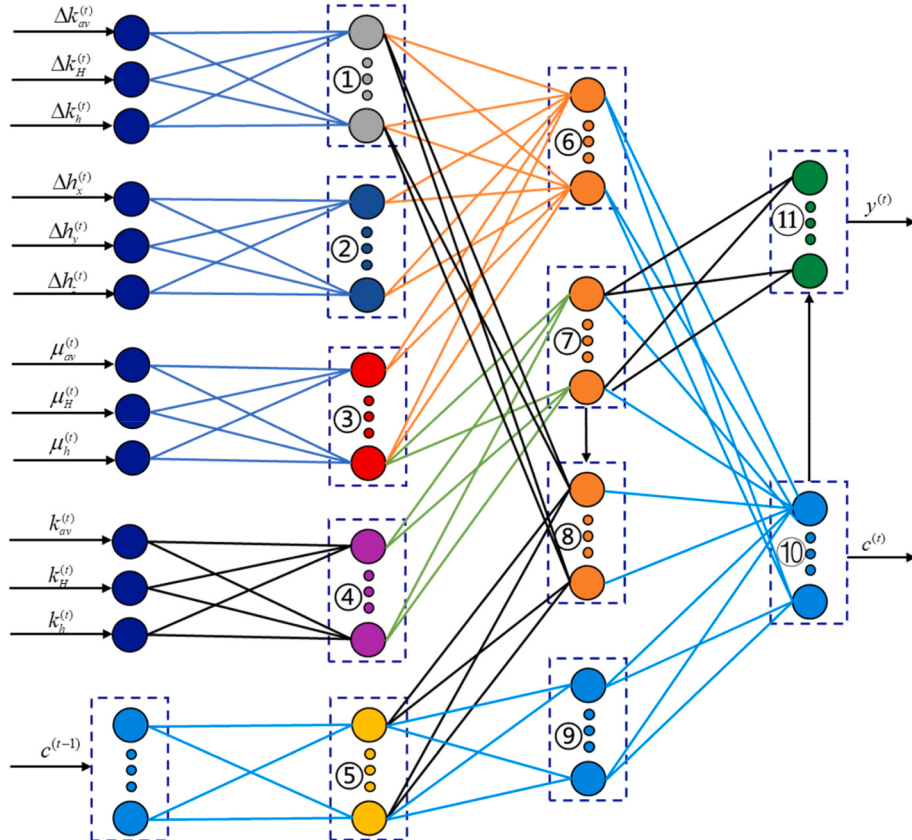


Fig. 4. The fundamental architecture of the improved LSTM algorithm model.

points on the X, Y, and Z coordinate axes and dividing these differences by the maximum (or reference) side length of the study area on the corresponding coordinate axes, respectively. $\mu^{(n)}$ represents the influence factor of geological structure on the regional ISSF of the measurement point n . This three-dimensional value based on the three key parameters, i.e. the average, maximum, and minimum horizontal LPCs, is accurately calculated by Eq. (12). $\Delta k^{(n)}$ represents the increment of the three types of side pressure coefficients at measurement point n , which is derived from the three types of side pressure coefficients calculated from the measured ISSF, minus the average value of the three types of side pressure coefficients of the Chinese DCS based on the statistics of Eqs. (1)–(3). $W_f^{(n)}$, $U_f^{(n)}$, $V_f^{(n)}$ are the weight matrices used to analyze the measurement point n , and $b_f^{(n)}$ is the bias value matrix used to analyze the measurement point n .

In the second hidden layer, the specific function form of the neuron in region ⑦ is written as

$$H^{(n)} = \sigma(W_H^{(n)}\mu^{(n)} + U_H^{(n)}k^{(n)} + b_H^{(n)}) \quad (17)$$

where $H^{(n)}$ is the output value of measuring point n with respect to the neurons in region ⑦. $W_H^{(n)}$ and $U_H^{(n)}$ are the weight matrices used to analyze the measurement point n , and $b_H^{(n)}$ is the bias value matrix used to analyze the measurement point n .

In the second hidden layer, the specific function form of the neuron in region ⑧ is written as

$$a^{(n)} = \tanh[W_a^{(n)}(c^{(n-1)} - H^{(n)}) + U_a^{(n)}\Delta k^{(n)} + b_a^{(n)}] \quad (18)$$

where $a^{(n)}$ is the output value of the measuring point n with respect to the neuron in region ⑧. $c^{(n-1)}$ denotes the long-term memory unit state accumulated up to measurement point $n-1$, which contains the long-term memory information of the ISSF data sequence from measurement point 1 up to measurement point $n-1$. This unit state is the output value calculated by the algorithmic model in the region of the $n-1$ measurement point, which is used to store and reflect the distribution law and change pattern in regional ISSF. $c^{(0)}$ is the initial long-term memory unit state of the algorithmic model, which is determined by a stochastic initialization process. By setting $c^{(0)}$, the algorithmic model is able to capture and accumulate the ISSF information subsequent measurement points more efficiently, thus maintaining high accuracy throughout the prediction process. $W_a^{(n)}$, $U_a^{(n)}$ are the weight matrices used to analyze the measurement point n , and $b_a^{(n)}$ is the bias value matrix used to analyze the measurement point n .

In the output layer, it is divided into two separate areas: region ⑨ and ⑩. The region ⑨ consists of 25 neurons that directly use a special type of data processing - multiplying and adding up element by element. Region ⑩ includes 116 neurons which use the activation function as shown in Eq. (15).

The specific function form of the region ⑩ neurons of the output layer is shown in Eq. (19). The function of this region is to update and adjust the long-term memory unit state by combining the product operation and linear weighting of the hidden layer outputs.

$$c^{(n)} = c^{(n-1)} \odot f^{(n)} + H^{(n)} \odot a^{(n)} \quad (19)$$

where $c^{(n)}$ denotes the long-term memory unit state accumulated up to measurement point n , which serves as the output of the output layer. \odot denotes the computational notation for the direct multiplication of two matrices at corresponding positions.

The specific function form of the region ⑩ neurons of the output layer is shown in Eq. (20).

$$y^{(t)} = \tanh(V_c c^{(t)} + V_H^t H^{(t)} + b_o) \quad (20)$$

where $y^{(n)}$ represents the loading conditions prediction accumulated up to the measuring point n . When the algorithmic model resolves the complete sequence of ISSF data at the measurement points, its output is

the predicted values of the ISSF loading conditions constructed in the geological model. $V_H^{(n)}$ is the bias value matrices used to analyze the measurement point n . V_c and b_o are the weight and bias value matrix in algorithmic model, respectively.

4. Verification of prediction effectiveness and discussion on accuracy of the methods

4.1. Example-based verification

To validate the accuracy of the improved LSTM algorithm, an example involving a plane-strain circular wellbore subject to anisotropic far-field stresses in deep saturated rock. The ISSF around the wellbore is predicted in terms of far-field stress levels based on algorithm, and the results are compared with the analytical solutions in the literature.^{44,45} The validation data set originates from the literature by Wu and Zhang (2012).⁴⁴ In the literature, the authors studied the mechanical responses around a wellbore subject a non-hydrostatic far-field stresses. The problem was decomposed into two sub-problems with isotropic and anisotropic far field stresses, which corresponds to Mode I and Mode II, respectively, by using the superposition principle. Then the analytical solutions were obtained by using the Laplace transformation and the solution in the time space was obtained by using the Stefest method. To validate the analytical model, the authors conducted a detailed comparison with the results obtained from the existing studies. To be more specific, the stress distribution in Mode 1 was compared with the results by Chen and Ewy (2005),⁴⁶ while the pore pressure changes in Mode 2 were compared with the results by Detournay and Cheng (1988).⁴⁵ The results show an excellent agreement between them, which confirms the accuracy of the analytical model proposed Wu et al.

The model is as shown in Fig. 5, the origin of the coordinate system is set to be at the center of the wellbore with a radius of r_w , internal pressure of p_w , and a temperature of T_w . The initial temperature and pore pressure of the surrounding rock are denoted as T_R and p_R respectively, and the maximum and minimum horizontal principal stresses in the surrounding rock are denoted as σ_H and σ_h , respectively. The parameters used for the numerical calculation are shown in Table 2.

The validation process of the algorithm is rigorous and systematic. First, the ISSF dataset was constructed based on the theoretical formulas in literature,^{47,48} with the far-field stresses as the inputs and the radial, tangential and axial stresses in the region within a radius of 0.9 m around the wellbore as the outputs. This dataset includes 16 sets of

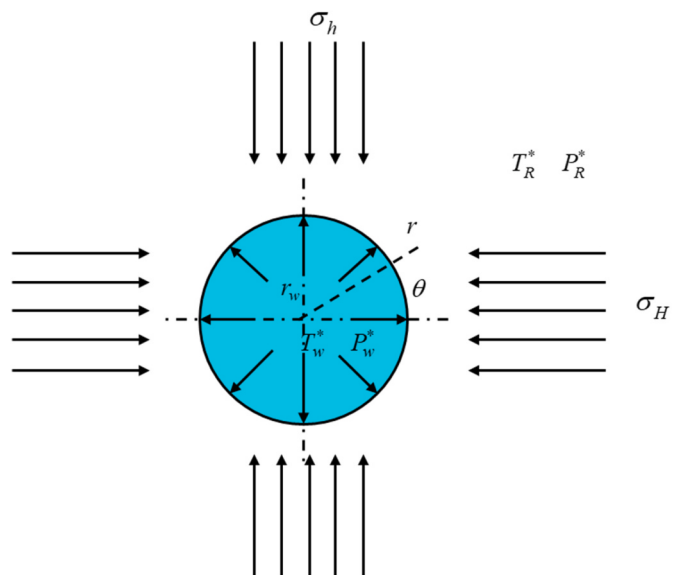


Fig. 5. Shaft wall model.

Table 2
Typical parameters for the calculations.⁴⁴

| Parameters | Values |
|---|----------------------|
| Fluid, rock mass density (kg/m^3) | 1000, 2700 |
| Fluid, rock specific heat (J/kg/K) | 4200, 1000 |
| Fluid, rock thermal conductivity (W/m/K) | 0.6, 2.4 |
| Rock permeability (mD) | 4.0×10^{-5} |
| Fluid viscosity (Pa·s) | 0.002 |
| Drained thermal expansion coefficient (1/K) | 5.0×10^{-6} |
| Undrained thermal expansion coefficient (1/K) | 10×10^{-6} |
| Biot coefficient | 0.47 |
| Initial pore pressure (Pa) | 7.8×10^6 |
| Well pressure (Pa) | 8.3×10^6 |
| Well temperature (K) | 323 |
| Initial temperature (K) | 333 |
| Shear modulus (Pa) | 1.5×10^{10} |
| Drained and undrained Poisson ratio | 0.25, 0.34 |
| Porosity | 0.01 |

samples, 15 of which are used for training and 1 used for validation. Then, the improved LSTM algorithm model is optimized with the training samples. Finally, the validation samples are brought into the optimization algorithm model in order to predict the stress in the surrounding rock, and a comparison between the predicted stresses and analytical solution is made, as shown in Fig. 6.

As shown in Fig. 6, the prediction accuracy for the radial, hoop and axial stresses are 99.194 %, 99.068 % and 99.205 %, respectively. The results show that improved LSTM algorithm used in this study has high accuracy.

4.2. Analysis of ISSF in Shanghai Temple mine

4.2.1. Geological profile

The tectonic outline of the Yingjun II wellfield is shown in Fig. 9, and the development of folds and faults in the wellfield evaluates the tectonic complexity as medium tectonic. The wellfield is located on the eastern flank of the New Shanghai Temple anticline, striking north-east, with a mostly gentle production pattern and a dip range of 5~15°. Along the tendency of the anticline, there are secondary folds Qingshuiying syncline and Qingshuiying anticline, and in the central part of the wellfield, the local inclination gradually increases due to the influence of the Qingshuiying syncline, and the inclination angle is 20~30°. According to the seismic data, there are totally 38 faults in this area, and

the faults with larger drop are in the fold belt of the east wing of the Qingshuiying syncline and the west wing of the Qingshuiying anticline at the boundary and in the middle of the wellfield. There are three faults with drop greater than 100 m, i.e. DF16, DF20 and DF37, two faults with drop less than 100 m greater than or equal to 50 m, i.e. DF17, DF39, and eight faults with drop less than 50 m greater than or equal to 20 m, i.e. DF12, DF14, DF15, DF18, DF19, DF21, F12 and DF30. The wellfield is fully covered by Holocene, Middle Pleistocene and Upper Pleistocene strata of the Quaternary and Tertiary strata in the Cenozoic, and the rock strata are dominated by sandstones, sedimentary debris, siltstones, mudstones, and so on. The aquifer is mainly water-filled by fissures, generally weakly to moderately water-rich, with poor groundwater recharge conditions and complex hydrogeological boundaries. The coal-bearing stratum is Jurassic Yan'an Formation, with an average thickness of 263.91 m. The mine is rich in coal seam resources, of which the eighth coal seam (referred to as the Coal 8) and the fifteenth coal seam (referred to as Coal 15) are particularly significant and are the focus of mining. The coal seams are generally gently inclined, trending nearly north-south, with an inclination angle of 5°~30°, and the top and bottom plates are mostly medium-hard fine-grained sandstone and soft siltstone.

The tectonic stress field in the wellfield area is variable and is subject to south-to-north thrusting during the Indo-Chinese period. In the early part of the Indo-Chinese sub-cyclone, regional uplift movements resulted in the absence of Early Triassic deposits, but the original tectonic pattern was not significantly altered, and the Middle and Upper Triassic units were deposited. In the late Indo-Chinese sub-cyclone, the large-scale uplift movement in the region caused the stripping away of the stratigraphy of the Extension Formation and the Early Jurassic Fuxian Formation, and a pseudo-consolidated contact between the Yan'an Formation and the underlying Extension Formation was obtained. During the Yanshan period, a series of north-west oriented geological formations were produced by a north-west-south-east oriented stress field. In the early part of the Yanshan Movement, the uplift movement deposited the Jurassic Middle Yan'an Formation, Zhiluo Formation and Anding Formation. In the middle stage of the Yanshan movement, the tectonic movement was intense, forming a series of folds and fractures with nearly north-south orientations, and deposited on top of the pre-existing strata with angular unconformity. In the late stage of the Yanshan movement, the strata were folded again and uplifted based on the previous tectonic pattern, after which the regional tectonics tended to stabilize. During the Xishan Movement, the south-west to north-east thrusting produced some near-north-south fault structures with right-lateral tension and torsion, as well as low-angle, wide and gentle folds along the right-lateral alignment. This was followed by strong uplift movements and depositional thicknesses of up to 3000 m. During the Quaternary and Paleoproterozoic, tectonic movements were relatively weak, with the strata slightly folded and fractured.

4.2.2. Geological modelling

As shown in Fig. 7, the modeling area for this study is the extent of a well-defined rectangular box that covers the critical upper area of the core zone of the Qingshuiying anticline in the central part of the well field, as well as the critical infrastructure within the area: the main well, the secondary well, the wind shaft, and the industrial plaza. This area has large normal fault, i.e. DF15 SF15 and DF20. The DF15 and SF15 large-scale fault zones strike northeast and dip northwest, with a dip of about 22°, a drop of less than 20 m, and a fault extension length of about 540 m, which has a certain cutting effect on the residual coal seams in the core of Qingshuiying anticline. The DF20 reverse fault gradually extends to the north and south ends, faulting the remnant Yan'an Formation strata in the core of the Qingshuiying anticline. The fault has a strike orientation of NE, inclination of SE, dip angle of about 34°, drop of 14 m, and fault extension length of about 180 m.

The stratigraphic and fault coordinates are collated by using Civil3D software and imported into ABAQUS software to form the geological model shown in Fig. 8. The geological model contains 9 layers with 7

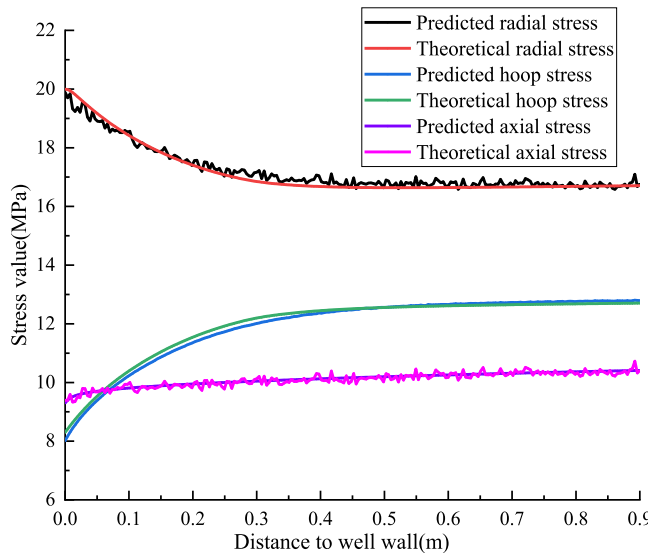


Fig. 6. Comparison of predicted and analyzed solutions for perimeter rock stresses.

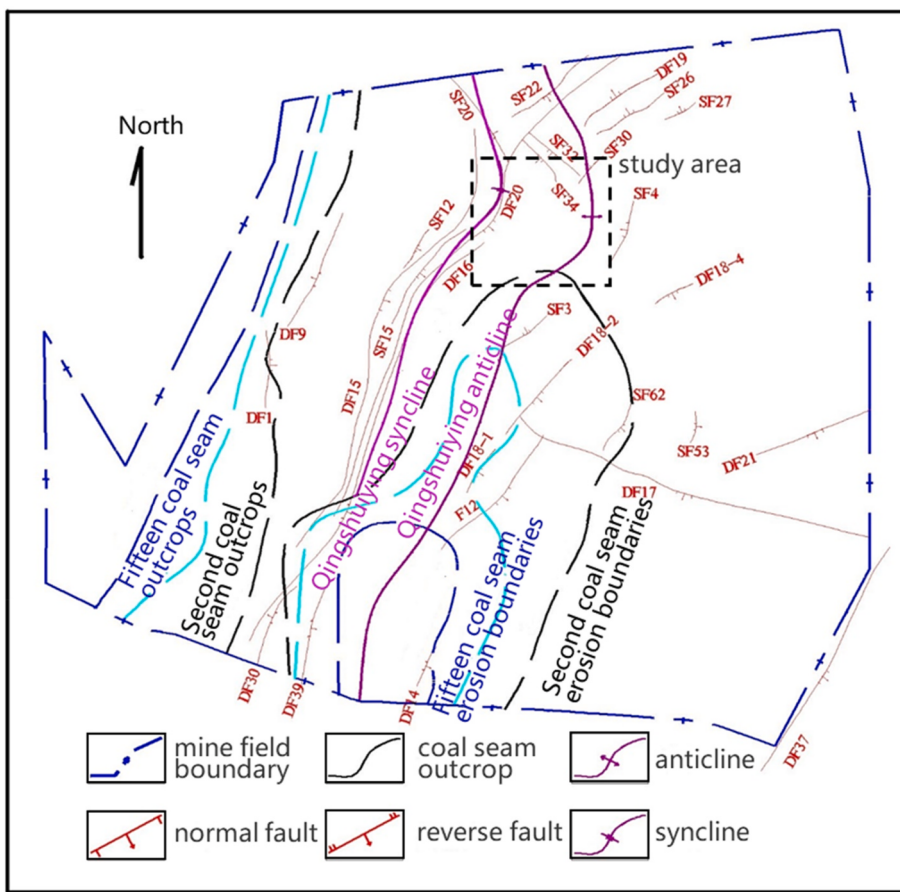


Fig. 7. The geological outline of the Yingjun II wellfield.

rock seams and 2 deep mineable coal seams (8th coal and 15th coal), and has three normal faults, i.e. DF15, SF15 and DF20. The geologic model is constructed according to a standard Cartesian coordinate system, where the Z-axis points vertically upward. At the surface level, the highest point corresponds to a Z-axis coordinate of up to 1360 m; while the very bottom of the model, at a depth of 1360 m below ground, has its Z-axis coordinate set to 0 m. The X-axis coordinate ranges from 4000 m to 6000 m, starts from the Qingshuiying syncline in the west and ends at the Qingshuiying anticline in the east. The Y-axis coordinates range from 0 to 2000 m, from 5600D6 exploration line in the south to 500 m north of the D10 exploration line in the north.

Given the complex and highly variable lithology of the field strata, the geological characteristics of the coal seams and geotechnical bodies are determined as listed in Table 3,⁴⁹ based on the experimental results of rocks at different depths and the mechanical properties at the engineering site.

4.2.3. Inversion of ISSF

When calculating the ISSF in the DCSA using ABAQUS software, the discontinuous loading models are implemented by writing subroutines such as umat and dload. The whole process of implementing the discontinuous intelligent inversion method proposed in this study is divided into the following four steps.

- (1) First, the lower surface of the geological model was completely fixed constrained, i.e., its displacement in all directions was restricted to ensure that the bottom of the model would not move due to external forces. Next, the upper surface of the model was set to be an unconstrained free surface, allowing it to respond freely to external loading or internal stress changes. Further, a normal constraint is imposed on a particular vertical surface of

the model. Specifically, on the surface located at the intersection of $X = 4000$ (hereinafter referred to as “boundary surface of $X = 4000$ ”), its displacement along the direction normal to that surface is fixed. Similarly, a similar normal constraint is applied to the vertical surface of the model at the intersection with $Y = 0$ (hereinafter referred to as “boundary surface of $Y = 0$ ”).

- (2) Based on Eqs. (7) and (8), 30 sets of discontinuous and nonlinear loading conditions are randomly designed. These conditions are designed to simulate the complex and variable tectonic stress in real engineering environments. Subsequently, these loads were applied to the two vertical interfaces of the model, i.e. one interface was perpendicular to the X -axis and located at $X = 6000$ (referred to as "boundary surface of $X = 6000$ "), and the other interface was perpendicular to the Y -axis and located at $Y = 2000$ (referred to as "boundary surface of $Y = 2000$ "). This setup ensures that the loads accurately simulate the mechanical effects in different directions, thus more realistically reflecting the complexity of the actual ISSF formation process. In addition, 30 sets of discontinuous self-gravity loads were further introduced to the whole model based on Eq (9). These loads are mainly used to simulate the self-gravitating stress field of the rock formation and characterize the possible local stress concentration or release phenomena inside the geological body.
 - (3) Based on 30 sets of numerical simulation results of the discontinuous loading model, the ISSF data at the location of the measurement points are used as input samples, while the loading model coefficients are used as output samples. The improved LSTM algorithm model was initialized, and intensive iterative training was carried out using the constructed sample dataset. During the training process of the improved LSTM algorithm model, the error variation curve is formed as shown in Fig. 9. As

training proceeds, the algorithmic model gradually demonstrates its powerful feature learning capability. It is able to automatically extract from the ISSF data those key features for predicting the loading conditions. To avoid overfitting that leads to the degradation of the algorithm's generalization capability, the optimization is terminated when the sample training error variation rate is less than 0.001 %, and the optimal algorithm model is obtained.

- (4) The measured ISSF data from the engineering site source into the optimization algorithm model, discontinuous and nonlinear loading conditions can be calculated, and its discontinuous loading model is able to simulate high-precision ISSF.

The compressive loadings on the boundary surface of $X = 6000$ in the geological model is denoted by σ_{x1} and σ_{x2} , with positive compressive stress in Pa. They are written as follows

$$\sigma_{x1} = \begin{cases} -108417.10 & z \in [1111.68, 1360] \cap y \in [0, 972.85] \\ -45062.45 & z \in [989.49, 1111.68] \cap y \in [0, 972.85] \\ -3.47z^2 + 19733.67z - 1048204.67 & z \in [856.63, 989.49] \cap y \in [0, 972.85] \\ -4.86z^2 + 27641.63z - 1468256.54 & z \in [691.21, 856.63] \cap y \in [0, 972.85] \\ -4.50z^2 + 25578.54z - 1358669.85 & z \in [609.07, 691.21] \cap y \in [0, 995.30] \\ -4.24z^2 + 24106.54z - 1280481.08 & z \in [0, 609.07] \cap y \in [0, 995.30] \end{cases} \quad (22)$$

$$\sigma_{x2} = \begin{cases} 1.39z^2 + 28776.76z + 823398.89 & z \in [1054.28, 1360] \cap y \in (972.85, 2000] \\ 1.48z^2 + 30484.95z + 1988997.99 & z \in [819.71, 1054.28] \cap y \in (972.85, 2000] \\ 1.12z^2 + 23177.71z + 1722251.36 & z \in [563.13, 819.71] \cap y \in (972.85, 2000] \\ 1.14z^2 + 23562.64z + 674205.75 & z \in [0, 563.13] \cap y \in (972.85, 2000] \end{cases} \quad (23)$$

$$\sigma_{yx} = -0.05z^3 + 23.06z^2 - 6653.67z + 1775.60 \quad z \in [0, 1360] \cap x \in [4000, 4813.27] \quad (27)$$

where the unit of the vertical coordinate, z (depth), and the north-south horizontal coordinate, y , and east-west vertical coordinate, x , is m.

The compressive loadings on the boundary surface of $Y = 2000$ in the geological model are denoted by σ_{y1} and σ_{y2} , with compressive stress in Pa

$$\sigma_{y1} = \begin{cases} 823589.07 & z \in [1192.23, 1360] \cap x \in [4000, 4763.42] \\ -2.26z^2 + 13812.50z - 66807.96 & z \in [954.82, 1192.23] \cap x \in [4000, 4763.42] \\ -11.04z^2 + 67413.75z - 3260302.49 & z \in [880.83, 954.82] \cap x \in [4000, 4763.42] \\ -11.76z^2 + 71834.87z - 3474118.93 & z \in [703.41, 880.83] \cap x \in [4000, 4763.42] \\ -4.57z^2 + 27914.67z - 1350025.17 & z \in [496.45, 703.41] \cap x \in [4000, 4763.42] \\ -2.28z^2 + 13896.90z - 672089.77 & z \in [0, 496.45] \cap x \in [4000, 4763.42] \end{cases} \quad (24)$$

$$\sigma_{y2} = \begin{cases} 7.26z^2 + 5453.82z + 729241.37 & z \in [1145.49, 1360] \cap x \in (4763.42, 6000] \\ 2.07z^2 + 1555.31z + 207963.39 & z \in [964.71, 1145.49] \cap x \in 4763.42, 6000] \\ 8.91z^2 + 6692.89z + 894919.90 & z \in [799.51, 964.71] \cap x \in (4763.42, 6000] \\ 7.78z^2 + 5845.61z + 781627.88 & z \in [0, 799.51] \cap x \in (4763.42, 6000] \end{cases} \quad (25)$$

The shear loadings on the boundary surfaces of $X = 6000$ and boundary surfaces of $Y = 2000$ in the geological model is denoted by τ_{xy} and τ_{yx} , with τ_{xy} positive along the Y -axis and τ_{yx} positive along the X -axis, and the unit is Pa.

$$\sigma_{xy} = -0.20z^2 + 314.03z - 1173.19 \quad z \in [0, 1360] \cap y \in [1024.64, 2000] \quad (26)$$

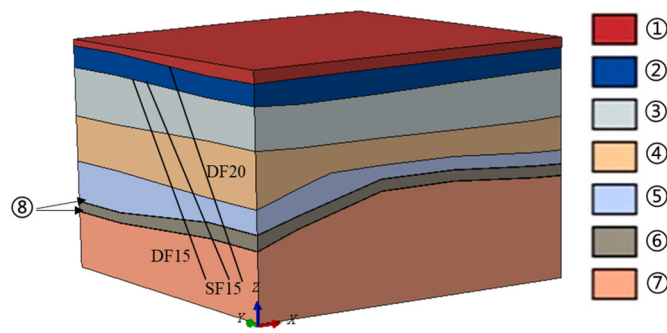


Fig. 8. Three-dimensional geological model for the mining area.

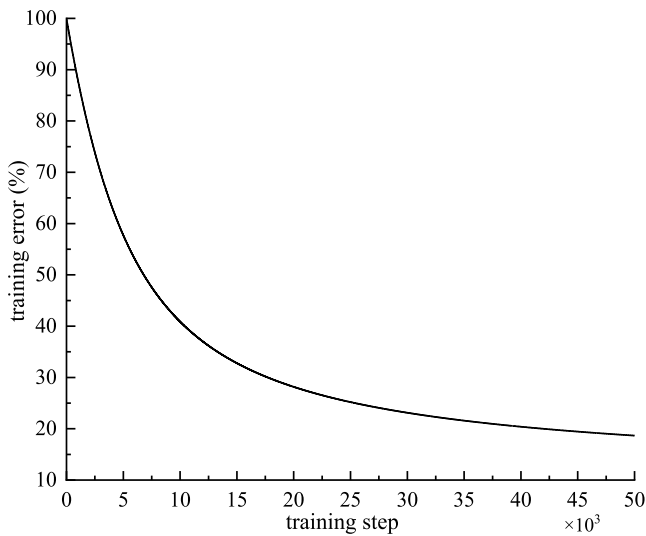


Fig. 9. Variation of error values during algorithm optimization learning.

and those predicted by the proposed method. It can be observed that they are in a good agreement with a statistical accuracy rate of 85.51 %, a high correlation coefficient of 0.984, and an average error value of only 0.985 MPa. However, significant errors were found in some data points such as the compressive stress in the X-direction for measurement segment No. 1, as well as the shear stress recorded at measurement points No. 9 to 13.

Regarding the issue of the inverted compressive stress value in the X-direction of measurement point 1 being higher than the actual value, it is mainly attributed to two major factors: the limitation in accuracy of the field measurement equipment and the simplified treatment of stratigraphic description in the numerical model. Specifically, due to the constraints of computer resources, the element mesh size in this area is set to 10 m, resulting in the selected target mesh element being not only excessively large in size but also relatively deep in position. Under the influence of Gaussian integration, this choice may have exacerbated the deviation in the calculation results, thereby generating an excessively

high compressive stress value. For the measurement points numbered 9 to 13, which are located within measurement hole No. 2, the shear stress values are generally below 0.10 MPa, which is extremely disproportionate to their burial depth exceeding 500 m. This indicates that significant errors may have occurred during the field measurements and the conversion process to shear stress. However, when using the improved LSTM algorithm proposed in this study, even in the presence of data with high noise levels, the algorithm is still able to improve accuracy to a certain extent. As verified in the subsequent discussion section, compared to the BPNN algorithm, the inversion error value of this algorithm is the lowest, which fully demonstrates its high precision and stability in inversion.

Fig. 10 shows the predicted maximum principal stress (MPS) distribution in the whole area. It is found that the MPS in the region range from 0 to 47.45 MPa. The vertical stratification of the ISSF in the shallow region is obvious, as is the horizontal banding of the ISSF in the deep region. The shallow ISSF is dominated by the horizontal direction and gradually transform to the vertical direction with depth increasing. In the deep core of the Qingshuiying backslope, the stress field magnitude increases, and the stress direction is deflected more. The ISSF in the limb region of the Qingshuiying anticline is attenuated, with a maximum stress attenuation of about 5 MPa. The maximum increase in the ISSF in the core region of the Qingshuiying anticline is about 8 MPa, and the direction of the MPS is about 45° along the vertical offset. The stress attenuation in the DF15 and SF15 fault zones is about 4 MPa with the direction of maximum stresses roughly perpendicular to fault strike, and the stress increase in the DF20 fault zone is about 5 MPa, but the regional extent of change is relatively small. This is consistent with the tectonic history in which the shallow strata were deposited more continuously, and the tectonic movements were relatively weak, whereas the deeper strata were subjected to strong Yanshan gyratory tectonic action, resulting in stratigraphic folding and fracturing. In conclusion, the regional ISSF has significant characteristics of coal mine sediment ability stratigraphic, and the inversion results are reasonable.

To further analyze the ISSF obtained from the intelligent algorithm inversion method, four typical profiles in the east-west and north-south directions are selected for analysis. The profiles of $Y = 300$ and $Y = 1600$ were selected for east-west direction, and the profiles of $X = 4800$ and $X = 5500$ were selected for the north-south direction.

Fig. 11 shows the MPS in the east-west profile with more geological formations. Here Fig. 11(a) and (b) are profiles of $Y = 300$ and $Y = 1600$, respectively. By comparing Fig. 11(a) and (b), the deep ISSF in the east-west direction is dominated by the faults tectonics, while the ISSF in the shallow region is more influenced by fold tectonics. As a fold structure extending from southwest to northeast, the ISSF in the core region of the Qingshuiying anticline has been slightly enhanced, with an average increase of about 3.6 MPa. The direction of the maximum horizontal principal stress is almost parallel to the fold slope plane (as shown in Fig. 11(a)), which demonstrates that the fold structure has a direct effect on the direction of the ISSF. The core region of the Qingshuiying syncline is truncated by the SF15 fault, and ISSF decreases by about 4.0 MPa. The direction of the maximum horizontal principal stress is no longer parallel to the fold slope plane, but rather is a deflected by about 45° (shown in Fig. 11(b)), which indicates that the faults have a stronger

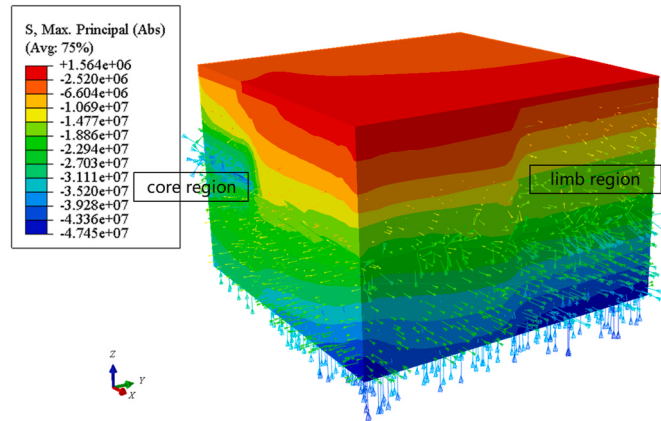
Table 3
Mechanical parameters of coal seam and rock soil layer.

| Number in figure | Stratigraphic sequence number | Density/(kg/m ³) | Young's modulus/MPa | Poisson's ratio | Friction angle/° | Cohesion yield Stress/MPa |
|------------------|-------------------------------|------------------------------|---------------------|-----------------|------------------|---------------------------|
| ① | First layer | 2200 | 3060 | 0.212 | 36.00 | 1.35 |
| ② | Second layer | 2250 | 5670 | 0.460 | 42.61 | 1.92 |
| ③ | Third layer | 2310 | 7220 | 0.235 | 40.02 | 2.17 |
| ④ | Fourth layer | 2310 | 7220 | 0.235 | 38.13 | 2.19 |
| ⑤ | Fifth layer | 2360 | 9905 | 0.232 | 40.02 | 2.17 |
| ⑥ | Sixthly layer | 2230 | 5600 | 0.184 | 42.61 | 1.92 |
| ⑦ | Seventh layer | 2270 | 5570 | 0.214 | 48.19 | 1.94 |
| ⑧ | Coal layer | 1540 | 5000 | 0.400 | 30.00 | 1.40 |

Table 4

Comparison of stress values at measurement points and inversion values.

| Number | Inverse value | | | | Measured value | | | | Error | | | |
|--------|-----------------|-----------------|-----------------|-----------------|-----------------|-----------------|-----------------|-----------------|-----------------|-----------------|-----------------|-----------------|
| | S _{xx} | S _{yy} | S _{zz} | S _{xy} | S _{xx} | S _{yy} | S _{zz} | S _{xy} | S _{xx} | S _{yy} | S _{zz} | S _{xy} |
| 1 | 10.02 | 7.92 | 5.27 | 2.02 | 6.46 | 6.74 | 5.64 | 2.04 | 55.17 % | 17.55 % | 6.64 % | 0.82 % |
| 2 | 11.47 | 10.71 | 7.11 | 2.53 | 9.12 | 9.51 | 7.74 | 2.80 | 25.77 % | 12.58 % | 8.11 % | 9.47 % |
| 3 | 13.06 | 13.22 | 8.78 | 3.11 | 12.42 | 12.83 | 9.80 | 2.99 | 5.16 % | 3.01 % | 10.38 % | 3.98 % |
| 4 | 13.61 | 14.52 | 10.59 | 3.51 | 13.90 | 14.37 | 11.29 | 3.36 | 2.06 % | 1.06 % | 6.21 % | 4.48 % |
| 5 | 15.17 | 16.04 | 12.90 | 4.21 | 17.22 | 17.82 | 13.96 | 4.28 | 11.91 % | 9.96 % | 7.60 % | 1.57 % |
| 6 | 20.03 | 21.37 | 14.91 | 4.61 | 18.39 | 19.08 | 15.46 | 4.90 | 8.89 % | 12.01 % | 3.55 % | 5.88 % |
| 7 | 20.80 | 22.21 | 16.21 | 4.91 | 20.69 | 21.38 | 16.64 | 4.89 | 0.54 % | 3.89 % | 2.57 % | 0.40 % |
| 8 | 7.91 | 4.20 | 4.58 | 0.05 | 6.79 | 3.28 | 4.17 | 0.06 | 16.44 % | 27.92 % | 9.85 % | 16.43 % |
| 9 | 10.37 | 5.62 | 6.92 | 0.05 | 9.09 | 5.01 | 6.26 | 0.07 | 14.08 % | 12.12 % | 10.60 % | 25.20 % |
| 10 | 11.83 | 7.08 | 9.56 | 0.07 | 12.22 | 6.19 | 8.05 | 0.11 | 3.19 % | 14.33 % | 18.80 % | 39.18 % |
| 11 | 14.73 | 8.53 | 12.06 | 0.07 | 16.35 | 8.87 | 11.03 | 0.13 | 9.91 % | 3.79 % | 9.35 % | 43.84 % |
| 12 | 21.83 | 12.27 | 16.11 | 0.04 | 19.70 | 11.16 | 13.41 | 0.15 | 10.79 % | 9.92 % | 20.13 % | 71.34 % |
| 13 | 24.67 | 13.74 | 18.71 | 0.01 | 22.68 | 13.83 | 15.50 | 0.15 | 8.76 % | 0.65 % | 20.70 % | 95.45 % |

**Fig. 10.** Inversion results of the full-domain MPS.

remodelling effect on the local ISSF. As shown in Fig. 11(a), the ISSF shows a relatively smooth state in the region where the DF15 and SF15 normal faults intersect. As the two faults continue to extend northward and gradually separate (as shown in Fig. 11(b)), the ISSF in the region of the two fault zones show a decreasing trend, which indicates that the tensile tectonic movements play a dominant role in the fault formation process. However, in the DF20 normal fault region, the significant attenuation of the ISSF is mainly attributed to the superposition of tensile and gravitational effects, and the attenuation is particularly prominent in the upper disk region, where the attenuation values are up to about 5 MPa.

An in-depth inversion analysis of the ISSF in the geotectonic region was carried out, and the intelligent inversion method demonstrated excellent performance. The advantage of this method lies in the fact that it effectively solves the problem of having to generalize geological formations due to the scale limitations of geological models by introducing a discontinuous loading model that can accurately characterize the ISSF of these generalized areas and provide effective ISSF data of the localized generalized areas for the improved LSTM algorithm model.

Fig. 12 shows the inferred MPS in the north-south profile with the discontinuous stratigraphic region. There Fig. 12(a) and (b) are for the profiles located at Y = 300 m and Y = 1600 m, respectively. In the core region of Qingshuiying syncline, the ISSF attenuates by around 2.5 MPa, which is smaller compared to the attenuation of the syncline in the east-west direction influenced by fault zones. The maximum horizontal principal stress in this region is nearly perpendicular to the fold slope plane. The ISSF exhibits significant discontinuities in the north-south direction, which is mainly attributed to the combined effects of sedimentary discontinuities and strong compressive tectonic movements in the geological history, compared to the weaker effects of shear tectonic

activities in the horizontal direction. In particular, in the discontinuous settlement zone close to the mined Coal 15, the ISSF of the top and bottom rock layers increased significantly compared with that of the surrounding rock at the same burial depth, with the maximum stress value as high as 40.20 MPa. The ISSF shows significant stratification effects and large fluctuations in the horizontal and vertical directions. Through exhaustive inversion analyses, the discontinuous distribution of ISSF in the north-south direction is extremely significant, which is consistent with the distribution law of the ISSF in the discontinuous coal strata in sedimentary rock layers. It indicates that the discontinuous intelligent inversion method shows high accuracy even when dealing with geological regions with complex discontinuous structures.

4.3. Discussion

To further validate the discontinuous intelligent inversion method developed in this study, and to explore the key factors causing the errors, the ISSFs obtained from the improved LSTM algorithm and the Back-propagation Neural Network (BPNN) are compared by using the continuous and discontinuous loading models. Both algorithms utilized exactly the same input and output parameter settings. The specific outcomes are shown in Fig. 13.

In Fig. 13, Methods 1 and 2 represent the improved LSTM and BPNN algorithms, respectively, based on the discontinuous loading model, and Methods 3 and 4 represent the improved LSTM and BPNN algorithms, respectively, based on the continuous loading model. In other words, Method 1 is the discontinuous intelligent inversion method proposed in this study. The proposed improved LSTM algorithms (Methods 1 and 3) significantly outperform the BPNN algorithms (Methods 2 and 4), whether based on the discontinuous or continuous loading model. Based on the numerical results of the discontinuous loading model, the improved LSTM algorithm has high inversion accuracy, with an average error of only 14.49 %, which is much lower than that of the BPNN algorithm (Method 2) with 93.25 %. This large difference not only demonstrates the excellent ability of the improved LSTM algorithm in dealing with nonlinear and discrete data, but also highlights its great potential in improving the accuracy of complex ISSF inversion. As for the continuous loading model, the improved LSTM algorithm (Method 3) still maintains a significant advantage, with an average error of 31.20 %, much lower than that of the BPNN algorithm (Method 4) with 128.28 %. This confirms the wide applicability and high stability of the improved LSTM algorithm on different VS-dimensional data. For the application of the same algorithm, the results based on the discontinuous loading model show higher accuracy. It is noteworthy that the continuous loading model fails to calculate the geological information that matches well with the shear stress at the measurement point when constructing the sample dataset, and this defect directly leads to a significant decrease in the accuracy in predicting the shear stress at the

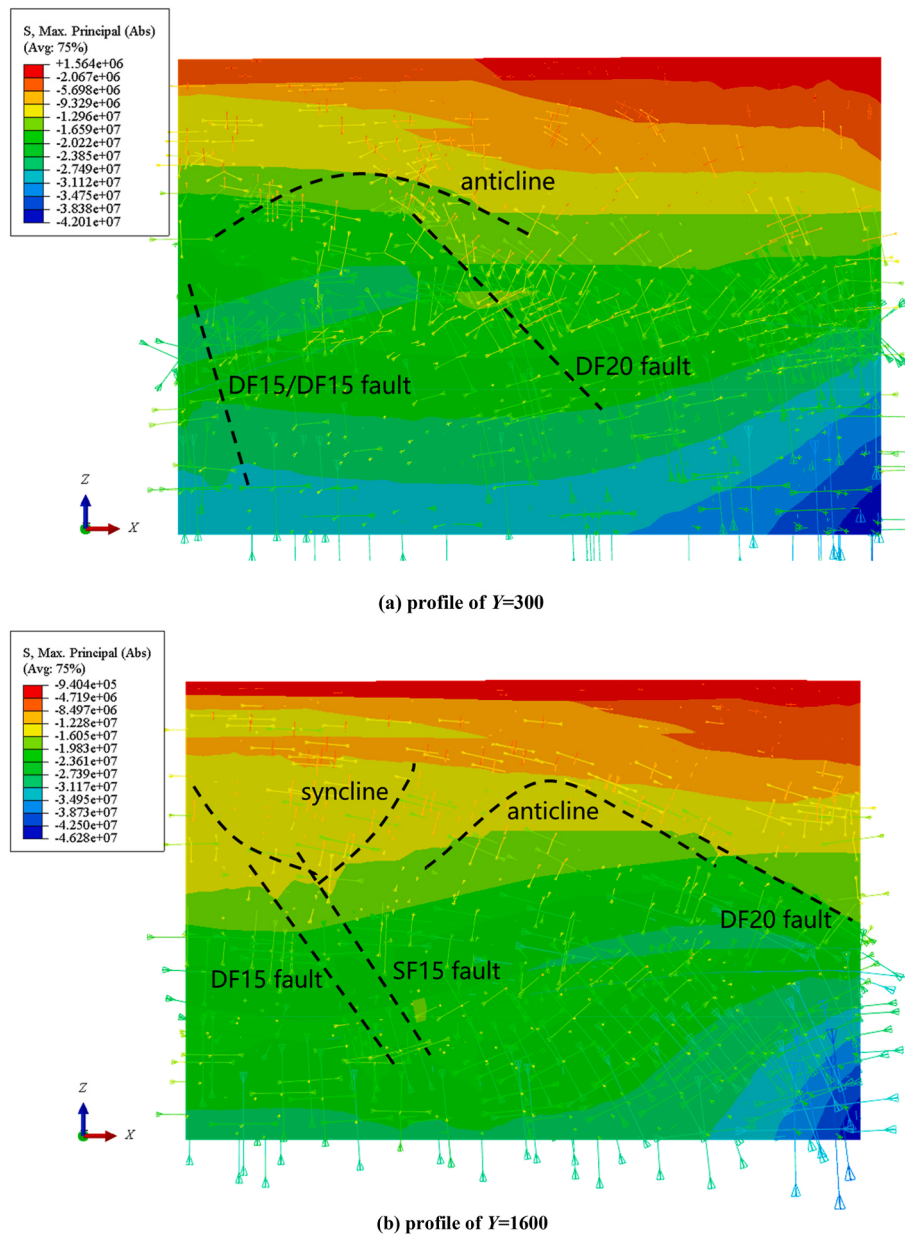


Fig. 11. MPS inversion results in the east-west profile.

measurement point using the improved LSTM algorithm. However, when using the BPNN algorithm, not only the prediction of shear stresses is significantly affected, even the inversion accuracy of partial positive stresses is significantly reduced. This indicates that the sample dataset constructed by the discontinuous loading model has a better match between its VC dimensions and the measured dataset. The BPNN algorithm is significantly limited in its accuracy when faced with complex sample datasets. In contrast, the long and short-term memory mechanism in the improved LSTM algorithm is fully activated in this scenario and its optimized network hierarchy effectively handles the complex sample dataset by means of multi-parameter cyclic learning, which enables the improved LSTM algorithm to have higher inversion accuracy.

Fig. 14 shows the reconstructed full domain MPS distributions for the three inversion methods (i.e. Method 2, Method 3, and Method 4), which are analyzed in detail in comparison with the inversion results of the discontinuous intelligent inversion method (Method 1), as shown in Fig. 10.

Fig. 14 shows that the discontinuous loading model has obvious

advantages when calculating the ISSF compared to the continuous loading model, and the results obtained by the BPNN algorithm are in agreement with the actual conditions to a certain degree. The computational bias of the continuous loading model in localised areas significantly affects the completeness of the sample dataset, leading to a significant reduction in the ISSF prediction accuracy of both inversion algorithms outside the coverage of the measurement points. Particularly, in the complex geotectonic region, such as the deep Qingshuiying anticline fault structure, the two inversion algorithms fail to adequately reflect the unique ISSF characteristics of the region, which leads to the prediction results contradicting with the strong geotectonic movement background of the region in the past. Fundamentally, the numerical results of the continuous loading model cannot fully characterize the complex and variable features of the actual ISSF, leading to insufficient VC dimensions for calculating the ISSF sample dataset. The two algorithms can only seek the local optimal solution in a limited subspace of information samples in the information-poor situation, and this "weak" solution can barely maintain a certain degree of accuracy in the vicinity

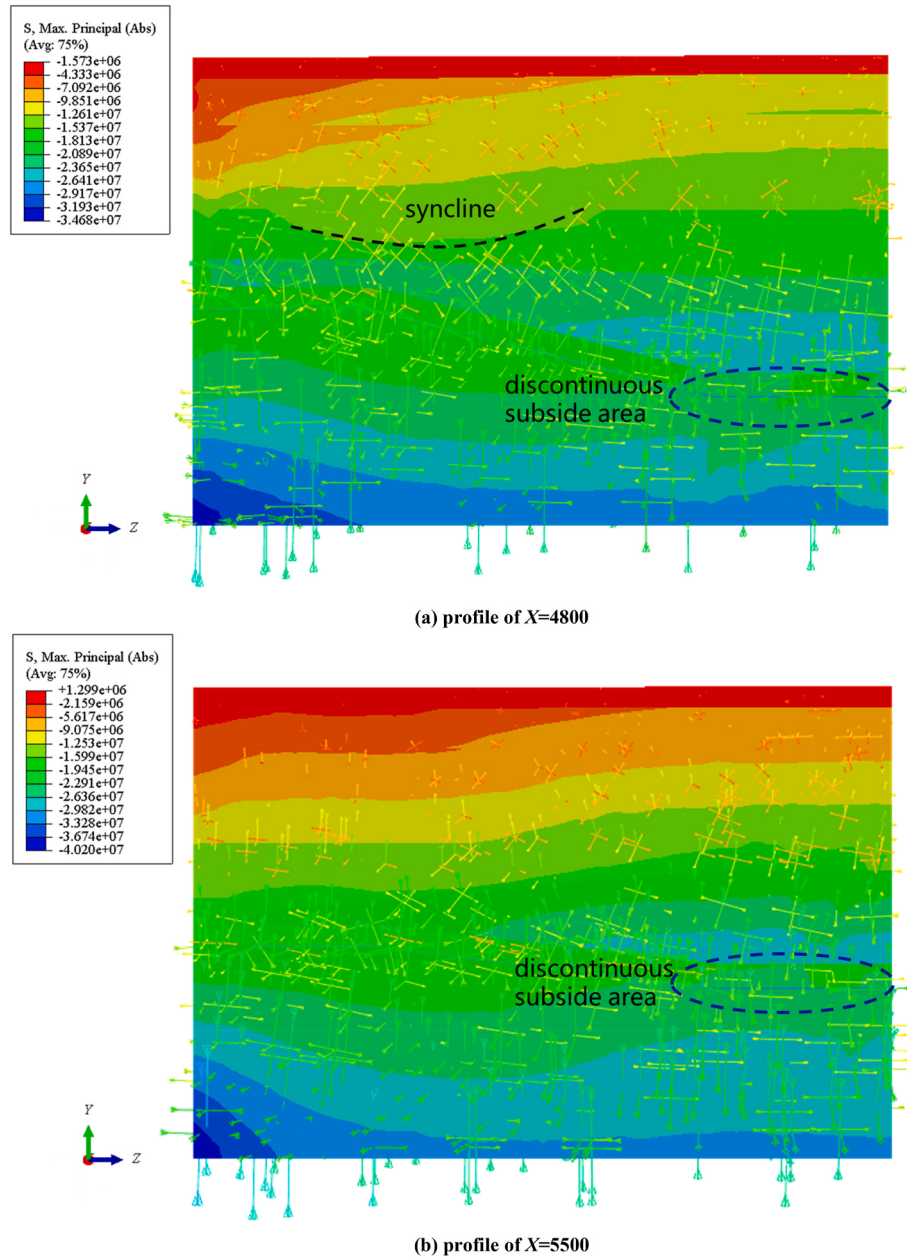


Fig. 12. MPS in the north-south profile.

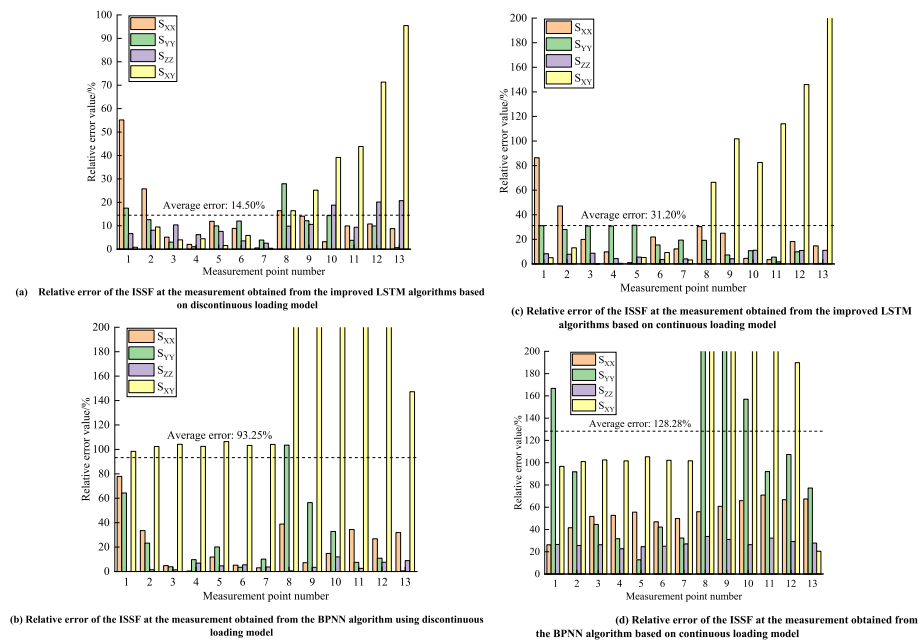


Fig. 13. Comparison of the inversion results between four methods.

of the measurement point, but once far away from the measurement point, the prediction results will be rapidly distorted.

By comparing Figs. 14 and 10, it can be seen that the stress increase in the core area of the anticline in Fig. 14 is not prominent, and on the contrary, a large zone of stress attenuation is observed in the fault zone area. This contradicts the actual situation described in the geological historical record, because theoretically, the late sedimentary strata would have compacted the area around the overlying faults, resulting in no large-scale stress attenuation zones in the area. In the inversion of the ISSF in DCSA, it is necessary to establish a tectonic loading pattern that coincides with each gyre period from the formation mechanism of the ISSF. The sample dataset generated by numerical computation using the discontinuous loading model has an eigenspace dimension that can highly approximate the eigenspace dimension of the actual measured sample dataset. Meanwhile, the improved LSTM algorithm proposed in this study demonstrates its unique advantages in dealing with complex geological data. The algorithm not only comprehensively considers the model error and generalization error, but also deeply mines the geological information embedded in the ISSF data at the measurement points through the structure of multi-level and multi-type neuron networks. This deep mining ability enables the algorithm to understand the complex structure of the deep ISSF more accurately, thus realizing an effective solution to the full-domain ISSF problem.

The discontinuous intelligent inversion algorithm proposed in this study, by integrating the discontinuous loading model with the improved LSTM algorithm, not only ensures the precision of the predicted results at the measurement points but also enhances the credibility of the predicted results across the entire study area. This innovative method shows great potential in applications across various critical fields, such as geological exploration, coal, and oil and gas resource development, aiding in increasing resource development efficiency and reducing potential risks.

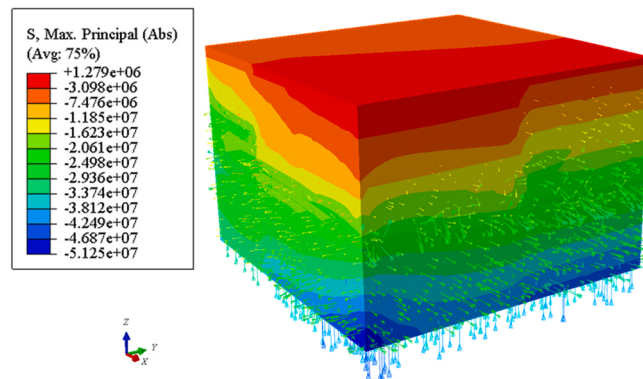
Although the new method performs well in most application scenarios, its performance still has certain limitations. Especially when dealing with monitoring or field-collected data that contain errors and noise, while the method can minimize the interference of these adverse factors to the greatest extent, it cannot completely eliminate errors and ensure the absolute accuracy of the predicted results. Therefore, future research will focus on further optimizing the algorithm and deeply integrating expertise in geomechanics with advanced filtering

techniques. Through this interdisciplinary integration, we anticipate being able to further enhance the stability and reliability of the predicted results to meet the higher standards required in related fields of research and practice.

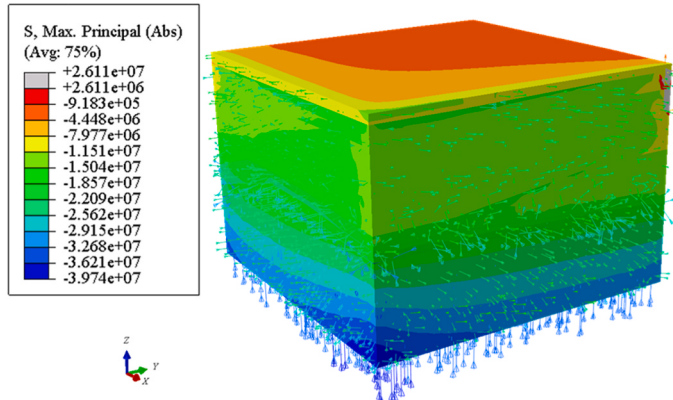
5. Conclusions

In this study, an intelligent inversion method is proposed for the complex nonlinear and discontinuous characteristics of the ISSF in DCSA. The method involves three key steps, i.e. construction of the discontinuous loading model, the fuzzy membership function to quantitatively characterize the degree of influence of geological tectonic on the ISSF, and the improvement of long short-term memory network algorithm, which realizes the accurate inversion of the ISSF in the DCSA of the Shanghai Temple Mine. The following conclusions are drawn:

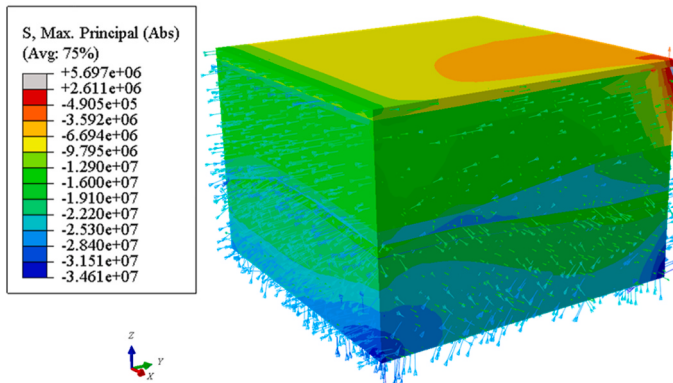
- (1) By comprehensively considering the formation and change mechanism of ISSF in different periods of geological history, three types of discontinuous loading conditions, namely, compressive, shear and self-weight, are constructed. The discontinuous loading model can ensure the calculation accuracy of ISSF in local geological tectonic regions, and significantly improve the accuracy and reliability of the sample dataset for numerical simulation of ISSF.
- (2) Aiming at the complex influence of different tectonics on the ISSF in deep geological bodies, a quantitative analysis method based on fuzzy mathematics is adapted. In view of the fact that discontinuous structures such as faults have a significant effect on the ISSF in localized areas but limited in overall scope, Gaussian-type fuzzy membership function is used to quantify the degree of their influence; while the effect of fold structures on the ISSF is gradual, homogeneous, and extensive, Cauchy-type fuzzy membership function is chosen to quantify it. This results in a geological structure influence function that quantifies the extent to which geological structures influence the average, maximum and minimum horizontal LPCs, increasing the data dimensions of the input samples to the improved LSTM algorithm model.
- (3) The proposed improved LSTM algorithm realizes the in-depth analysis of geological information by integrating multidimensional inputs (such as the degree of influence from geological



(a) MPS obtained from the BPNN algorithm based on discontinuous loading model calculations



(b) MPS obtained from the improved LSTM algorithms based on continuous loading model



(c) MPS obtained from the BPNN algorithm based on continuous loading model calculations

Fig. 14. Inversion results of MPS between four methods.

structures, LPCs and their increments, and the spacing of measurement points) of geological formations on the ISSF at the measurement points. The algorithm design focuses on the balance between model error and generalization ability, and also deeply explores the geological features in the ISSF data with the help of multi-level and multi-type activation functions. By taking the planar strain borehole model of a circular borehole in saturated rock as a case study, the algorithm demonstrates its excellent data parsing and prediction ability with a prediction accuracy of more than 99 % in the deep ISSF.

- (4) The ISSF in Shanghai Temple Mine predicted based on the discontinuous loading model show that the improved LSTM algorithm has the highest inversion accuracy, reaching 85.51 %. In contrast, based on the numerical simulation results of continuous loading model, the inversion accuracy of the BPNN algorithm is significantly lower than that of the improved LSTM algorithm. Therefore, it proves the effectiveness and high accuracy of the discontinuous intelligent inversion method proposed in this study, which provides a powerful support for the ISSF analysis and safety assessment in DCSA.

CRediT authorship contribution statement

Jiaxing Zhou: Writing – original draft, Methodology. **Bisheng Wu:** Writing – review & editing. **Yuanxun Nie:** Data curation, Conceptualization. **Haitao Zhang:** Software.

Funding

This research is under the support of the National Natural Science Foundation of China (Grant No. 52371279), the Open Research Fund Program of the State Key Laboratory of Hydroscience and Engineering of Tsinghua University (Grant No. sklhse-2023-D-02) and the Program for International Exchange and Cooperation in Education by the Ministry of Education of the People's Republic of China (Grant No. 57220500123).

Declaration of competing interest

The authors declare that they have no known competing financial interests or personal relationships that could have appeared to influence the work reported in this paper.

Data availability

No data was used for the research described in the article.

References

- Xie HP. Research review of the state key research development program of China: deep rock mechanics and mining theory. *J China Coal Soc.* 2019;44(5):1283–1305. <https://doi.org/10.13225/j.cnki.jccs.2019.6038> (In Chinese).
- Liu T, Li M, Zou Q, Li J, Lin M, Lin B. Crack instability in deep coal seam induced by the coupling of mining unloading and gas driving and transformation of failure mode. *Int J Rock Mech Min.* 2023;170, 105526. <https://doi.org/10.1016/j.ijrmms.2023.105526>.
- Siwek S. Earth tides and seismic activity in deep coal mining. *Int J Rock Mech Min.* 2021;148, 104972. <https://doi.org/10.1016/j.ijrmms.2021.104972>.
- Jiang Y, Pu L, Du F, et al. *Intra-Craton Faults Characteristics, Development and its Hydrocarbon Accumulation Significance in Mesozoic Strata at Southwestern Ordos Basin*. China: Geological Journal; 2024. <https://doi.org/10.1002/gj.5085>.
- Liu J, Yang H, Wu X, Liu Y. The in situ stress field and microscale controlling factors in the Ordos Basin, central China. *Int J Rock Mech Min.* 2020;135, 104482. <https://doi.org/10.1016/j.ijrmms.2020.104482>.
- Tao M, Li X, Wu C. Characteristics of the unloading process of rocks under high initial stress. *Comput Geotech.* 2012;45:83–92. <https://doi.org/10.1016/j.comgeo.2012.05.002>.
- Tao M, Li X, Wu C. 3D numerical model for dynamic loading-induced multiple fracture zones around underground cavity faces. *Comput Geotech.* 2013;54:33–45. <https://doi.org/10.1016/j.comgeo.2013.06.002>.
- Han H, Fukuda D, Liu H, et al. Combined finite-discrete element modellings of rockbursts in tunnelling under high in-situ stresses. *Comput Geotech.* 2021;137, 104261. <https://doi.org/10.1016/j.comgeo.2021.104261>.
- Yi C, Johansson D, Greberg J. Effects of in-situ stresses on the fracturing of rock by blasting. *Comput Geotech.* 2018;104:321–330. <https://doi.org/10.1016/j.comgeo.2017.12.004>.
- Kaiser PK, Kim BH. Characterization of strength of intact brittle rock considering confinement-dependent failure processes. *Rock Mech Rock Eng.* 2015;48:107–119. <https://doi.org/10.1007/s00603-014-0545-5>.
- Cai M, Peng H. Advance of in-situ stress measurement in China. *J Rock Mech Geotech.* 2011;3(4):373–384. <https://doi.org/10.3724/SP.J.1235.2011.00373>.
- Song S, Feng X, Liao C, Cai D, Liu Z, Yang Y. Measures for controlling large deformations of underground caverns under high in-situ stress condition-A case study of Jinping I hydropower station. *J Rock Mech Geotech.* 2016;8(5):605–618. <https://doi.org/10.1016/j.ijrmge.2016.06.002>.
- Zamani B. Geodynamics and tectonic stress model for the Zagros fold-thrust belt and classification of tectonic stress regimes. *Mar Petrol Geol.* 2023;155, 106340. <https://doi.org/10.1016/j.marpetgeo.2023.106340>.
- Kang H, Zhang X, Si L, Wu Y, Gao F. In-situ stress measurements and stress distribution characteristics in underground coal mines in China. *Eng Geol.* 2010;116 (3-4):333–345. <https://doi.org/10.1016/j.enggeo.2010.09.015>.
- Li X, Chen J, Ma C, et al. A novel in-situ stress measurement method incorporating non-oriented core ground re-orientation and acoustic emission: a case study of a deep borehole. *Int J Rock Mech Min.* 2022;152, 105079. <https://doi.org/10.1016/j.ijrmms.2022.105079>.
- Ziae M, Fazaelizadeh M, Tanha AA, Sharifzadegan A. Estimation of the horizontal in-situ stress magnitude and azimuth using previous drilling data. *Petroleum.* 2023;9 (3):352–363. <https://doi.org/10.1016/j.petlm.2023.02.006>.
- Xie HP. Research concept and expected results of “Deep rock mechanics and mining theory”. *Eng. Sci. Technol.* 2023;49(2):1–16. <https://doi.org/10.15961/j.sjuese.201700025> (In Chinese).
- Sheorey PR. A theory for in-situ stresses in isotropic and transversely isotropic rock. *Int J Rock Mech Min & Geomech Abstr.* 1994;31(1):23–34. [https://doi.org/10.1016/0148-9062\(94\)92312-4](https://doi.org/10.1016/0148-9062(94)92312-4).
- Martínez-Garzón P, Heibach O, Bohnhoff M. Contemporary stress and strain field in the Mediterranean from stress inversion of focal mechanisms and GPS data. *Tectonophysics.* 2020;774, 288286. <https://doi.org/10.1016/j.tecto.2019.228286>.
- Papanastasiou P, Kyriacou A, Sarris E. Constraining the in-situ stresses in a tectonically active offshore basin in Eastern Mediterranean. *J Petrol Sci Eng.* 2017;149:208–217. <https://doi.org/10.1016/j.petrol.2016.10.033>.
- Qian L, Yao T, Mo Z, et al. GAN inversion method of an initial in situ stress field based on the lateral stress coefficient. *Sci Rep.* 2021;11(1), 21825. <https://doi.org/10.1038/s41598-021-01307-1>.
- Song ZF, Sun YJ, Lin X. Research on in situ stress measurement and inversion, and its influence on roadway layout in coal mine with thick coal seam and large mining height. *Geotech Geol Eng.* 2018;36:1907–1917. <https://doi.org/10.1007/s10706-017-0427-1>.
- Li F, Wang J, Brigham JC. Inverse calculation of in situ stress in rock mass using the surrogate-model accelerated random search algorithm. *Comput Geotech.* 2014;61: 24–32. <https://doi.org/10.1016/j.compgeo.2014.04.003>.
- Pei Q, Ding X, Liu Y, Lu B, Huang S, Fu J. Optimized back analysis method for stress determination based on identification of local stress measurements and its application. *Bull Eng Geol Environ.* 2019;78:375–396. <https://doi.org/10.1007/s10064-017-1118-0>.
- Zhang S, Hu A, Wang C. Three-dimensional inversion analysis of an in situ stress field based on a two-stage optimization algorithm. *J Zhejiang Univ - Sci A.* 2016;17 (10):782–802. <https://doi.org/10.1631/jzus.A1600014>.
- Yu D, Yang Z, Guo Y, Yang Y, Wang B. Inversion method of initial geostress field in coal mine based on FLAC3D transversely isotropic model. *J China Coal Soc.* 2020;45 (10):3427–3434. <https://doi.org/10.13225/j.cnki.jccs.2019.1242> (In Chinese).
- Meng W, He C, Chen ZQ, et al. Application of ridge regression in inversion of initial geostress field of rock mass. *Rock Soil Mech.* 2021;42(4):1156–1169. <https://doi.org/10.16285/j.rsm.2020.1317> (In Chinese).
- Angelier J. Inversion of field data in fault tectonics to obtain the regional stress-III. A new rapid direct inversion method by analytical means. *Geophys J Int.* 1990;103(2): 363–376. <https://doi.org/10.1111/j.1365-246X.1990.tb01777.x>.
- Khoshkhogh S, Orozova-Bekkevold I, Mosegaard K. Evolution of the stress and strain field in the Tyrrhenian Sea during the Post-Challenger deposition and seismic inversion of fault zone using informed-proposal Monte Carlo. *Appl. Comput. Geosci.* 2022;14, 100085. <https://doi.org/10.1016/j.acags.2022.100085>.
- Wang TX, Zheng WH, Liang SJ. Numerical simulation of regional stress field under complex geological condition. *Appl Mech Mater.* 2011;90:531–536. <https://doi.org/10.4028/www.scientific.net/AMM.90-93.531>.
- Brown ET, Hoek E. Trends in relationships between measured in-situ stresses and depth. *Int J Rock Mech Min & Geomech Abstr.* 1978;15(4):211–215. [https://doi.org/10.1016/0148-9062\(78\)91227-5](https://doi.org/10.1016/0148-9062(78)91227-5).
- Hoek E, Brown ET. *Underground Excavations in Rock*. Underground Excavations in Rock. vol. 10. CRC Press; 1980, 9781482288926. <https://doi.org/10.1201/9781482288926>.
- McGarr A. On the state of lithospheric stress in the absence of applied tectonic forces. *J Geophys Res Solid Earth.* 1988;93(B11):13609–13617. <https://doi.org/10.1029/JB093iB11p13609>.
- Chen Z, Zhou Z, He C, Jiang C, Wang B, Li T. Influence of faults on the geo-stress field distribution and damage evolution mechanism of fracture zones. *Bull Eng Geol Environ.* 2023;82(5):173. <https://doi.org/10.1007/s10064-023-03194-4>.
- Zhao H, Ma F, Xu J, Guo J. In situ stress field inversion and its application in mining-induced rock mass movement. *Int J Rock Mech Min.* 2012;53:120–128. <https://doi.org/10.1016/j.ijrmms.2012.05.005>.
- Li L, Jiang Q, Huang Q, Xiang T, Liu J. Advances in stability analysis and optimization design of large underground caverns under high geostress condition. *Deep Eng. Eng.* 2024, 100113 <https://doi.org/10.1016/j.deepre.2024.100113>.
- Shi W, Dong S, Hu J. Neotectonics around the Ordos Block, North China: a review and new insights. *Earth Sci Rev.* 2020;200, 102969. <https://doi.org/10.1016/j.earscirev.2019.102969>.
- Benitez-Diaz D, Garcia-Quesada J. *Learning algorithm with Gaussian membership function for fuzzy RBF neural networks*. International Workshop on Artificial Neural Networks. Berlin, Heidelberg: Springer Berlin Heidelberg; 1995:527–534. <https://doi.org/10.1007/BF0094973.219>.
- Civanlar MR, Trussell HJ. Constructing membership functions using statistical data. *Fuzzy Set Syst.* 1986;18(1):1–13. [https://doi.org/10.1016/0165-0114\(86\)90024-2](https://doi.org/10.1016/0165-0114(86)90024-2).
- Raj D, Gupta A, Garg B, Tanna K, Rhee FCH. Analysis of data generated from multidimensional Type-1 and Type-2 fuzzy membership functions. *IEEE Trans Fuzzy Syst.* 2018;26(2):681–693. <https://doi.org/10.1109/TFUZZ.2018.2838024>.
- Heaton J, Ian goodfellow, yoshua Bengio, and aaron courville: deep learning. *The mit press.* 2016;19(1):305–307. <https://doi.org/10.1007/s10710-017-9314-z>, 800 pp, isbn: 0262035618. *Genetic programming and evolvable machines*, 2018.
- Wu S, Zhao G, Wu B. Real-time prediction of the mechanical behavior of suction caisson during installation process using GA-BP neural network. *Eng Appl Artif Intell.* 2022;116, 105475. <https://doi.org/10.1016/j.engappai.2022.105475>.
- Sharma S, Sharma S, Athaiya A. Activation functions in neural networks. *Data Sci.* 2017;6(12):310–316.
- Wu B, Zhang X, Jeffrey RG, Wu B. A semi-analytic solution of a wellbore in a non-isothermal low-permeability porous medium under non-hydrostatic stresses. *Int J*

- Solid Struct.* 2012;49(13):1472–1484. <https://doi.org/10.1016/j.ijisolstr.2012.02.035>.
45. Detournay E, Cheng AHD. Poroelastic response of a borehole in a non-hydrostatic stress field. *Int J Rock Mech Min & Geomech Abstr.* 1988;25(3):171–182. [https://doi.org/10.1016/0148-9062\(88\)92299-1](https://doi.org/10.1016/0148-9062(88)92299-1).
46. Chen G, Ewy RT. Thermo-poro-elastic effect on wellbore stability. *SPE J.* 2005;10(2):121–129. <https://doi.org/10.2118/89039-PA>.
47. Coussy O. A general theory of thermo-poro-elastoplasticity for saturated porous materials. *J. Trans. Porous Med.* 1989;4(3):281–293. <https://doi.org/10.1007/BF00138040>.
48. Wu B, Gamage RP, Zhang X, Jeffrey RG, Wang X. An analytical thermo-poro-elasticity model for the mechanical responses of a wellbore and core during overcoring. *Int J Rock Mech Min.* 2017;98:141–158. <https://doi.org/10.1016/j.ijrmms.2017.07.006>.
49. Fei L, Jiaxing Z, Jinan W. Method of nonlinear in-situ stress construction with deep multi-field coupling. *J China Coal Soc.* 2021;46(S1):116–129. <https://doi.org/10.13225/j.cnki.jccs.2020.0857> (In Chinese).